

# 1 The third RADIATION transfer Model Intercomparison (RAMI) 2 exercise: Documenting progress in canopy reflectance models

J-L. Widlowski,<sup>1</sup> M. Taberner,<sup>1</sup> B. Pinty,<sup>1</sup> V. Bruniqnel-Pinel,<sup>2</sup> M. Disney,<sup>3</sup> R. Fernandes,<sup>4</sup> J-P. Gastellu-Etchegorry,<sup>5</sup> N. Gobron,<sup>1</sup> A. Kuusk,<sup>6</sup> T. Lavergne,<sup>1</sup> S. Leblanc,<sup>7</sup> P. E. Lewis,<sup>3</sup> E. Martin,<sup>5</sup> M. Möttus,<sup>6</sup> P. R. J. North,<sup>8</sup> W. Qin,<sup>9</sup> M. Robustelli,<sup>1</sup> N. Rochdi,<sup>4</sup> R. Ruiloba,<sup>2</sup> C. Soler,<sup>10</sup> R. Thompson,<sup>11</sup> W. Verhoef,<sup>12</sup> M. M. Verstraete,<sup>1</sup> D. Xie,<sup>13</sup>

## 3 Abstract.

4 The RADIATION transfer Model Intercomparison (RAMI) initiative benchmarks canopy  
5 reflectance models under well-controlled experimental conditions. Launched for the first  
6 time in 1999 this triennial community exercise encourages the systematic evaluation of  
7 canopy reflectance models on a voluntary basis. The first phase of RAMI focused on doc-  
8 umenting the spread among radiative transfer (RT) simulations over a small set of pri-  
9 marily 1-D canopies. The second phase expanded the scope to include structurally com-  
10 plex 3-D plant architectures with and without background topography. Here sometimes  
11 significant discrepancies were noted which effectively prevented the definition of a reli-  
12 able “surrogate truth” – over heterogeneous vegetation canopies – against which other  
13 RT models could then be compared. The present paper documents the outcome of the  
14 third phase of RAMI, highlighting both the significant progress that has been made in  
15 terms of model agreement since RAMI-2, and the capability of/need for RT models to  
16 accurately reproduce local estimates of radiative quantities under conditions that are rem-  
17 iniscent of *in situ* measurements. Our assessment of the self-consistency, the relative- and  
18 absolute performance of 3-D Monte Carlo models in RAMI-3 supports their usage in the  
19 generation of a “surrogate truth” for all RAMI test cases. This development then leads  
20 1) to the presentation of the ‘RAMI On-line Model Checker’ (ROMC), an open-access  
21 web-based interface to evaluate RT models automatically, and 2) to a reassessment of  
22 the role, scope and opportunities of the RAMI project in the future.

## 1. Introduction

23 Space-borne observations constitute a highly appropri-  
24 ate source of information to quantify and monitor earth  
25 surface processes. The quality/confidence that may be  
26 associated with the outcome of interpretation and assim-  
27 ilation efforts of these data streams, however, relies heav-  
28 ily on the actual performance of the available modelling  
29 tools. This understanding has led to a series of model  
30 intercomparison projects (MIP) aiming either to docu-  
31 ment the spread of currently available simulation mod-  
32 els, or, else to assess and benchmark the quality of their  
33 simulation results, *e.g.*, *Henderson-Sellers et al.* [1995];  
34 *Gates et al.* [1998]; *Dirmeyer et al.* [1999]; *Pinty et al.*  
35 [2001]; *Latif et al.* [2001]; *Cahalan et al.* [2005]; *Ran-*  
36 *gasayi et al.* [2005]. Among these MIPs the RADIATION  
37 transfer Model Intercomparison (RAMI) activity focuses  
38 on the proper representation of the radiative processes  
39 occurring, in vegetated environments, in the optical do-  
40 main of the solar spectrum. The design and launch of  
41 the first phase of RAMI occurred approximately in par-  
42 allel with that of the ‘Intercomparison of 3-D Radiation  
43 Codes’ (I3RC) activity which deals with the correct rep-  
44 resentation of the radiative properties of 3-D cloud fields  
45 (<http://i3rc.gsfc.nasa.gov/>). Both MIPs collaborate  
46 actively and share their evaluation methodologies in or-  
47 der to overcome the difficulties associated with model

---

<sup>1</sup>European Commission, DG Joint Research Centre,

48 benchmarking in the absence of absolute reference stan-  
49 dards.

50

51 The first phase of RAMI (RAMI-1) was launched in  
52 1999. Its prime objective was to document the variabil-  
53 ity that existed between canopy reflectance models when  
54 run under well controlled experimental conditions [*Pinty*  
55 *et al.*, 2001]. The positive response of the various RAMI-  
56 1 participants and the subsequent improvements made  
57 to a series of radiative transfer (RT) models promoted  
58 the launching of the second phase of RAMI (RAMI-2)  
59 in 2002. Here the number of test cases was expanded  
60 to focus further on the performance of models dealing  
61 with structurally complex 3-D plant environments. The  
62 main outcomes of RAMI-2 included 1) an increase in the  
63 number of participating models, 2) a better agreement  
64 between the model simulations in the case of the struc-  
65 turally simple scenes inherited from RAMI-1, and 3) the  
66 need to reduce the sometimes substantial differences be-  
67 tween some of the 3-D RT models over complex hetero-  
68 geneous scenes [*Pinty et al.*, 2004b]. The latter issue  
69 was noted as one of the challenges that future intercom-  
70 parison activities would have to face, since the reliable  
71 derivation of some sort of “surrogate truth” data set will  
72 not be possible in the absence of any agreement between  
73 these RT models. This, in turn, would then imply that—  
74 except in some simple special cases—the evaluation of RT  
75 model simulations can not proceed beyond their mutual  
76 comparison due to the general lack of absolute reference  
77 standards.

78

79 This paper will describe the outcome of the third phase  
80 of RAMI (RAMI-3). Section 2 will provide an overview  
81 of the organisation and model evaluation protocol em-  
82 ployed during RAMI-3. Section 3 documents how the  
83 performance of RT models—when applied to the various  
84 baseline scenarios inherited from RAMI-1—improved be-

---

Institute for Environment and Sustainability, Global  
Environment Monitoring Unit, TP 440, via E. Fermi 1,  
I-21020 Ispra (VA), Italy.

<sup>2</sup>NOVELTIS, Parc Technologique du Canal, 2 avenue de  
l’Europe, 31520 Ramonville Saint-Agne, France.

<sup>3</sup>Department of Geography, University College London,  
26 Bedford Way, London, WC1H 0AP, UK, and NERC  
Centre for Terrestrial Carbon Dynamics.

<sup>4</sup>Canada Centre for Remote Sensing, Natural Resources  
Canada, 588 Booth Str., Ottawa, ONT K1A 0Y7, Canada

<sup>5</sup>Centre d’Etudes Spatiales de la BIOSphère, 18 av.  
Edouard Belin, bpi 2801, 31401 Toulouse cedex 9, France

<sup>6</sup>Tartu Observatory, 61602 Tõravere, Estonia.

<sup>7</sup>Centre Spatial John H. Chapman, 6767, Route de  
l’Aéroport, Saint-Huber, Québec, Canada, J3Y 8Y9.

<sup>8</sup>Climate and Land-Surface Systems Interaction Centre,  
Department of Geography, University of Wales Swansea,  
Singleton Park, Swansea, SA2 8PP, UK.

<sup>9</sup>Science Systems and Applications, Inc., Greenbelt,  
Maryland, USA.

<sup>10</sup>ARTIS, INRIA Rhône-Alpes, 655, Avenue de l’Europe,  
38334 Saint Ismier Cedex, France

<sup>11</sup>Alachua Research Institute, Alachua, Florida, USA.

<sup>12</sup>National Aerospace Laboratory NLR, P.O. Box 153  
8300 AD Emmeloord, Netherlands

<sup>13</sup>Research Center for Remote Sensing and GIS, School of  
Geography, Beijing Normal University, Xijiekouwai Street  
19, Beijing, China.

85 tween RAMI-2 and RAMI-3. Section 4 documents the  
86 outcome of model simulations for the newly proposed ex-  
87 periments and measurement types in RAMI-3. Section 5  
88 summarises the main achievements and issues observed  
89 during RAMI-3 and introduces the “Rami On-line Model  
90 Checker” (ROMC), a web-based tool intended to auto-  
91 mate the process of RT model benchmarking. Section 5  
92 also describes possible roadmaps for the future develop-  
93 ment of the RAMI initiative.

## 2. The third phase of RAMI

94 The third phase of RAMI was officially launched at  
95 the end of March 2005. Scientists from around the world  
96 with an interest in canopy RT modelling were invited to  
97 participate in this triennial benchmarking exercise. A  
98 dedicated website (<http://rami-benchmark.jrc.it/>)<sup>1</sup>  
99 provided detailed descriptions regarding the structural,  
100 spectral and illumination conditions of the test cases  
101 proposed for RAMI-3. Prior to going public, each one  
102 of these experiments and measurements had been ap-  
103 proved by the RAMI advisory body, a small group of well-  
104 known scientists in the field of radiative transfer mod-  
105 elling and/or model intercomparison activities. RAMI-  
106 3 included and built upon the various experiments and  
107 measurements proposed during earlier phases of RAMI  
108 (see Section 2.1 in *Pinty et al.* [2001] and Section 2 in  
109 *Pinty et al.* [2004b]). Overall, the number of simulation  
110 scenarios grew by 37% with respect to RAMI-2, which  
111 led to two separate submission deadlines, namely, July  
112 30<sup>th</sup> 2005 for all RT simulations pertaining to struc-  
113 turally homogeneous vegetation canopies and December  
114 15<sup>th</sup> 2005 for all those simulations relating to structurally  
115 heterogeneous test cases. As was the case during pre-  
116 vious phases of RAMI, the collection of the submitted  
117 RT model results and their detailed analysis were per-  
118 formed at the Joint Research Centre (JRC) of the Eu-  
119 ropean Commission in Ispra, Italy. Two public presen-  
120 tations describing the outcome of this community effort  
121 were delivered, the first one—dealing with homogeneous  
122 test cases only—was given during the 9<sup>th</sup> International  
123 Symposium on Physical Measurements and Signatures in  
124 Remote Sensing (ISPMSRS) in Beijing, China (October  
125 2005), and the second one—including also the heteroge-  
126 neous test cases—at the 4<sup>th</sup> International workshop on  
127 multi-angular measurements and models (IWMMM-4) in  
128 Sydney, Australia (March 2006).

129  
130 Table 1 lists the models that participated in RAMI-  
131 3, the main publications describing these models and  
132 the names and affiliations of their operators. Also  
133 indicated are the corresponding modelling approaches  
134 that are used in order to simulate the radiation  
135 transfer. These include Monte Carlo (MC) tech-  
136 niques associated with forward/reverse ray-tracing meth-  
137 ods (*Drat*, *FLIGHT*, *frat*, *raytran*, *Rayspread* and  
138 *Sprint3*) or radiosity approaches (*RGM* and *Hyemalis*),  
139 purely analytical formulations (*2-Stream*), as well  
140 as, a large number of hybrid techniques, that com-  
141 bine one or more of the above with numerical,  
142 stochastic and/or geometric optical approaches (*ACRM*,  
143 *DART*, *1/2-discret*, *FRT*, *MAC*, *MBRF*, *Sail++*, *4SAIL2*,  
144 *5Scale*). More detailed information on the participat-  
145 ing models can be found on the RAMI website under  
146 [http://rami-benchmark.jrc.it/HTML/RAMI3/MODELS/M](http://rami-benchmark.jrc.it/HTML/RAMI3/MODELS/MODELS.php)  
147 [ODELS.php](http://rami-benchmark.jrc.it/HTML/RAMI3/MODELS/MODELS.php). Most of the participants received substantial  
148 feedback on the performance of their model(s) both as  
149 a result of phases 1 and 2, and in the case of obvious  
150 errors/deviations also during phase 3 of RAMI. Conse-

151 quently, all results presented below refer to the latest and  
152 most up-to-date version of these models. It is important  
153 that prospective users of these models ensure that they  
154 have access to the most recent version of these codes, as  
155 the performance information provided here may not be  
156 representative of, or applicable to, earlier versions.  
157

158 One of the traits of RAMI is to increase the number  
159 of test cases by including a few new experiments (and  
160 measurements) from one phase to another. This strategy  
161 serves a dual purpose, namely, a) to allow the evaluation  
162 of RT models under an increasingly comprehensive set of  
163 structural, spectral and also illumination conditions, and  
164 b) to tailor new sets of RAMI experiments and measure-  
165 ments around scientific questions emerging in the context  
166 of RT modelling and the quantitative interpretation of  
167 remotely sensed data. Indeed, such an approach guar-  
168 antees that every phase will contain at least some test  
169 cases for which the simulation results cannot be known  
170 *a priori*. Within RAMI-3 the following new experiments  
171 were proposed: 1) a conservative scattering scenario for  
172 the heterogeneous “floating spheres” test cases originally  
173 introduced during RAMI-1, 2) a “coniferous forest” scene  
174 analogous to the Gaussian-hill canopy introduced during  
175 RAMI-2 but without the topography, and 3) a “birch  
176 stand” populated with trees of variable sizes and spec-  
177 tral properties – intended primarily to enhance the de-  
178 gree of structural realism amongst the RAMI test cases.  
179 The new experiments complement those introduced dur-  
180 ing earlier phases of RAMI, which focused primarily on  
181 structurally homogeneous vegetation canopies (both in  
182 the solar domain and under conservative scattering con-  
183 ditions) but included also a small set of structurally het-  
184 erogeneous plant canopies (see Section 2.1 in *Pinty et al.*  
185 [2001] and Section 2 in *Pinty et al.* [2004b]). Exhaustive  
186 documentation on the spectral and structural properties  
187 of the various plant canopies (including the exact posi-  
188 tion and orientation of individual leaves in the scenes with  
189 discrete foliage representations, as well as the precise lo-  
190 cation of all tree-like objects in the scene) were accessible  
191 to the participants via the RAMI website. It was, how-  
192 ever, left to the participants themselves to choose what  
193 level of detail their model required in order to represent  
194 at best the proposed canopy scenes.  
195

196 Similar to previous phases of RAMI, participants were  
197 encouraged to generate a standard set of 11 measure-  
198 ments for every test case. These measurements in-  
199 clude the total spectral Bidirectional Reflectance Factor  
200 (BRF), in both the principal and the cross plane, together  
201 with the corresponding contributions due to the single-  
202 uncollided radiation scattered once by the soil only, the  
203 single-collided radiation by the leaves or trees only, and  
204 the radiation multiply collided by the leaves/trees/soil  
205 system. Three flux quantities were also routinely asked  
206 for, namely, the spectral albedo of the canopy (*i.e.*, the  
207 directional hemispherical reflectance), the total transmis-  
208 sion down to the underlying background, and, the total  
209 absorption of radiation in the vegetation layer. In ad-  
210 dition to these standard measurements, RAMI-3 intro-  
211 duced two new measurement types, that applied, how-  
212 ever, only to selected test cases. The first of these was a  
213 local transmission transect measurement that was asked  
214 for the “birch stand” experiment in order to assess the  
215 ability of RT models to simulate *in-situ* measurement sit-  
216 uations. Similarly, a horizontal flux measurement was  
217 proposed for the “real-zoom-in” scene, that was first  
218 introduced during RAMI-2 (section 2.2 in *Pinty et al.*  
219 [2004b]), in order to document the performance of RT

220 models when estimating the magnitude of horizontal pho-  
221 ton transport at various spatial resolutions in a struc-  
222 turally heterogeneous canopy environment. Almost all  
223 the RAMI measurements, whether directional or hemi-  
224 spherical, had to be carried out with respect to a refer-  
225 ence plane located at the top of canopy height level.

226  
227 Overall a total of 464,816 (2,112) individual BRF  
228 (flux) simulations were received at the JRC. In order  
229 to pursue the analysis of these data beyond a mere vi-  
230 sual comparison a protocol is needed that permits the  
231 quantitative evaluation of RT model simulations despite  
232 the lack of absolute reference standards (*i.e.*, in general  
233 the true solution is not known). *Oreskes et al.* [1994],  
234 and many others since, maintain that—under these lat-  
235 ter conditions—the complete validation/verification of a  
236 model is quite impossible, and that any such endeavour  
237 should focus instead on showing the opposite, that is,  
238 the onset of flaws in a model’s behaviour. RAMI thus  
239 proposes a three-step procedure to identify incongruous  
240 RT models: 1) by assessing the absence of inconsistencies  
241 in the internal RT formulation of a model, 2) by verify-  
242 ing the accurate and reliable performance of a model in  
243 the limited number of cases where analytical solutions  
244 are available, and 3) by comparing the output of a model  
245 against a “surrogate truth” that is to be established from  
246 credible candidates within the ensemble of available RT  
247 simulations. Obviously the latter will only be meaning-  
248 ful if sufficient consensus exists among the simulation re-  
249 sults of RT models, in particular those that are known to  
250 minimise the number of simplifications/approximations  
251 in their radiative transfer formulation. The objective of  
252 this three-step procedure thus lies in identifying RT mod-  
253 els that deviate from the norm rather than boosting the  
254 credibility of those models that do not differ. In fact,  
255 conformity with the anticipated outcome in each one of  
256 the above steps is not proof of a model’s physical cor-  
257 rectness. Hence any claims regarding the credibility of a  
258 model’s performance should be avoided, or—if they have  
259 to be made—should always be limited to the set of pre-  
260 scribed conditions under which the models were actually  
261 tested.

262  
263 In general, RT simulation models are rarely completely  
264 amiss, nor, totally correct for that matter, but tend to lie  
265 somewhere in between these two extremes. The quality of  
266 their simulations is often subject to the degree by which  
267 a given set of experimental conditions satisfies the struc-  
268 tural, spectral and/or radiative premises on which the  
269 models are based. In the context of RAMI, for example,  
270 models often do not share the same internal representa-  
271 tion or “image” of the prescribed canopy structure<sup>2</sup>. Such  
272 architectural deviations may often form the basis for sub-  
273 sequent differences in simulation results – as will be seen  
274 in sections 3 and 4. In addition to possible (structure and  
275 illumination related) differences in the starting premises  
276 of RT models, the precise manner in which certain RT  
277 quantities are simulated may also vary, *e.g.*, the width of  
278 the solid angle over which BRFs are computed may vary.  
279 The identification of suitable limits describing the thresh-  
280 old between valid and invalid models thus has to account  
281 for these idiosyncrasies, and should preferably be formu-  
282 lated in conjunction with criteria relating to the usage of  
283 these models. For example, by incorporating the abso-  
284 lute calibration accuracy of current space borne sensors  
285 and/or the anticipated quality of state-of-the-art atmo-  
286 spheric correction schemes into the evaluation scheme. In  
287 the next section the above three-step invalidation proce-  
288 dure will be applied to an ensemble of RAMI test cases for

289 which analytical solutions are available in a few isolated  
290 cases, and so-called “surrogate truths” may be derived  
291 for others, *e.g.*, *Pinty et al.* [2001, 2004b].

### 3. The RAMI baseline scenarios

292 All the forward-mode experiments that were proposed  
293 during RAMI-1 have featured in subsequent phases of  
294 the RAMI activity. These “baseline scenarios” can be  
295 subdivided into two separate architectural classes: The  
296 first one consists of structurally homogeneous canopies  
297 that feature finite-sized (discrete) or point-like (turbid)  
298 foliage elements that are randomly distributed within the  
299 volume of a horizontally infinite vegetation layer bounded  
300 by some top-of-canopy (TOC) level, as well as a lower  
301 flat background surface. The second category relates  
302 to structurally heterogeneous “floating spheres” environ-  
303 ments where the (discrete or turbid) foliage elements are  
304 randomly distributed within a series of spherical volumes  
305 that are themselves freely floating above an underlying  
306 flat background surface (for a graphical depiction see the  
307 inlaid pictures in Figure 1). In both categories the direc-  
308 tional scattering properties of the foliage and background  
309 are Lambertian, and the orientation of the foliage ele-  
310 ments follow predefined leaf normal distributions (LND),  
311 *i.e.*, *Bunnik* [1978] and *Goel and Strelak* [1984]. By vary-  
312 ing the illumination conditions, as well as the number,  
313 size, orientation and spectral properties of the foliage  
314 elements in the canopy (*idem* for the background bright-  
315 ness) up to 52 structurally homogeneous and 8 “floating  
316 spheres” baseline scenarios were defined. In the struc-  
317 turally homogeneous case, a “purist corner” was included  
318 where the spectral leaf and soil properties are such as to  
319 test model performance in the limit of conservative scat-  
320 tering conditions, *i.e.*, the soil brightness ( $\alpha = 1$ ) and  
321 the single-scattering albedo ( $r_L + t_L = 1$ ) are unity, and  
322 the leaf reflectance ( $r_L$ ) is equal to the leaf transmittance  
323 ( $t_L$ ).

324  
325 Figure 1 provides examples of the spread between  
326 the various RT models that participated in the base-  
327 line scenarios during RAMI-3. Shown are bidirectional  
328 reflectance factor (BRF) simulations along the principal  
329 (top panels) and orthogonal (bottom panel) planes  
330 for structurally homogeneous (left panels) and heteroge-  
331 neous “floating spheres” (right panels) canopies. The top  
332 panels feature finite-sized disc-shaped foliage elements of  
333 infinitesimal thickness (radius 0.1 m), whereas the bot-  
334 tom panels relate to turbid medium canopies, *i.e.*, having  
335 infinitesimally small but oriented scatterers. The spectral  
336 properties of the canopy constituents in the top (bottom)  
337 panels are typical for vegetation and bare soils in the red  
338 (NIR) spectral domain. The illumination zenith angle  
339 ( $\theta_i$ ) was set to  $20^\circ$  in all these cases. The panels of Fig-  
340 ure 1 exemplify the degree and variability of agreement  
341 between the various participating models. In particular,  
342 in the case of the structurally homogeneous test cases  
343 it is only the BRF simulations of the MBRF model in the  
344 turbid medium case (lower left panel), and, to a lesser ex-  
345 tent, the ACRM model in the discrete case (top left panel)  
346 that are different. The deviations of the MBRF model  
347 in the NIR may be largely explained by its usage of a  
348 “two-stream” approximation when estimating the mutli-  
349 ple collided BRF component. At the same time the agree-  
350 ment between the FLIGHT, drat, Rayspread, raytran,  
351 and Sprint3 Monte Carlo models is striking for both the  
352 homogeneous and heterogeneous test cases. Somewhat  
353 different from these 5 models—and each other—are the  
354 simulation results for DART, MAC, FRT, 4SAIL2, and 5Scale

355 in the turbid and/or discrete “floating spheres” test cases.

356  
357 Despite the visually noticeable dispersion of some of  
358 the model contributions in Figure 1, one should—in  
359 general—refrain from speculative guesses about potential  
360 outliers without a careful examination of the exact con-  
361 ditions under which the various models were executed.  
362 One of the first aspects to verify is the faithful repre-  
363 sentation of the prescribed architectural canopy char-  
364 acteristics. It is now well accepted that multi-angular  
365 observations are sensitive to the structure of a given  
366 canopy target, *e.g.*, *Gerard and North* [1997]; *Widlowski*  
367 *et al.* [2001]; *Lovell and Graetz* [2002]; *Chopping et al.*  
368 [2003]; *Chen et al.* [2003]; *Rautiainen et al.* [2003]. By  
369 the same token, deviations from the structural charac-  
370 teristics of a given RAMI scene may thus translate itself  
371 into the model-simulated magnitude (and shape) of the  
372 TOC BRF field. During RAMI-3 almost all of the par-  
373 ticipating models differed in their structural premises—  
374 either systematically or occasionally—from those pre-  
375 scribed on the RAMI website. For example, the **ACRM**  
376 and **MBRF** models both use elliptical equations [*Campbell*,  
377 1990] rather than beta-functions or geometric formula-  
378 tions to describe the LNDs of the foliage elements; **DART**  
379 approximates the “floating spheres” by a series of small  
380 cubes; **Hyemalis** reduced the physical dimensions of the  
381 proposed scenes to deal with internal computer memory  
382 requirements; **MAC**, **FRT** and **5Scale** assume a statistical—  
383 that is, random—spatial distribution of the objects in a  
384 scene rather than implementing the spatially explicit lo-  
385 cations prescribed on the RAMI website; **MBRF** uses rect-  
386 angular leaves rather than disc-shaped ones; **RGM** emulates  
387 leaf shapes by aggregating small triangular primitives;  
388 and the **Sprint3** model always uses statistical distribu-  
389 tions (rather than deterministic placements) of the foliage  
390 elements. These structural deviations—which are often  
391 motivated by the need for elegant and speedy solutions  
392 to the RT equation—may, however, become relevant in  
393 an intercomparison exercise like RAMI.

394  
395 *Widlowski et al.* [2005] recently showed that vegeta-  
396 tion canopies with identical domain-averaged state vari-  
397 able values but different structural representations will,  
398 in general, yield different multi-angular BRF patterns.  
399 In the context of RAMI, one may thus expect differ-  
400 ences to occur between RT models featuring exact rep-  
401 resentations of the prescribed canopy structures and 1)  
402 improved/expanded versions of essentially plane-parallel  
403 RT models in simulations over structurally heterogeneous  
404 canopy targets, or, 2) RT models that rely implicitly  
405 on 3-D plant structures (*i.e.*, Geometric Optical models)  
406 when applied to structurally homogeneous test cases. For  
407 these reasons the **MAC (4SAIL2)** model, which utilises a pa-  
408 rameterised formalism to distribute vegetation elements  
409 (gaps) within each elevation of its (one or two layer) veg-  
410 etation canopy representation, may deviate from the RT  
411 quantities simulated using models that make use of the  
412 actual location of vegetation elements in the heteroge-  
413 neous RAMI test cases. Similarly, the simulations of the  
414 **5Scale** model in the context of 1-D canopies have not  
415 been included in this manuscript.

416  
417 In order to obtain a comprehensive indication of the  
418 performance of a RT model in forward mode, it is essen-  
419 tial to run it on as large an ensemble of structurally and  
420 spectrally different canopy scenarios as possible – with-  
421 out, however, compromising the structural premises on  
422 which its internal canopy representation is based. Thus,  
423 the greater the degree of realism and the larger the struc-

424 tural diversity of the available number of RAMI test cases  
 425 is, the more indicative the observed BRF deviations be-  
 426 tween the various RT models and/or some “surrogate  
 427 truth” will become. Last but not least, one should also  
 428 note that the performance of many 1-D and 3-D RT mod-  
 429 els could always be improved through the usage of more  
 430 precise numerical integration schemes, as well as, larger  
 431 numbers of ray trajectories in the case of some of the MC  
 432 models. Such a “tuning” of model performances would,  
 433 however, be of little interest to model users if 1) the pub-  
 434 lically available versions of these computer codes cannot  
 435 deliver these accuracies, and 2) the computation times to  
 436 achieve such accuracies become prohibitive in the daily  
 437 usage of the models.

438  
 439 When constrained to evaluate model simulations in the  
 440 absence of any absolute reference standard or “truth”, as  
 441 is the case with RAMI, *Pinty et al.* [2001] argued that  
 442 RT model benchmarking on the basis of statistical mo-  
 443 ments, derived from the entirety of participating models,  
 444 may be biased in the presence of outliers. Instead they  
 445 proposed a relative evaluation scheme where the simu-  
 446 lations of individual models are compared against those  
 447 from all other participating models over as large as pos-  
 448 sible a set of conditions. In this way, RT models that  
 449 are consistently different from others can be identified  
 450 [*Pinty et al.*, 2004b]. The same authors also note that  
 451 internal inconsistencies in one or more submodules of a  
 452 given RT model may compensate each other and lead  
 453 to apparently correct overall BRF estimates. They thus  
 454 recommend the evaluation of BRF components as well as  
 455 the total BRFs generated by a model. In the following,  
 456 the three-step invalidation procedure from section 2 will  
 457 be applied to both the homogeneous and heterogeneous  
 458 baseline scenarios of RAMI-3. More specifically, subsec-  
 459 tion 3.1 will investigate the internal self-consistency of  
 460 the models that participated in the baseline scenarios of  
 461 RAMI-3. Subsection 3.2 then looks at RT model per-  
 462 formance in situations where exact analytical solutions  
 463 are available. Finally, subsection 3.3 documents various  
 464 aspects of relative model intercomparison with respect  
 465 to the discrete homogeneous and the “floating spheres”  
 466 baseline scenarios.

### 3.1. Model self-consistency

467 It is difficult to offer meaningful interpretations as to  
 468 why the output of a given RT model may be different  
 469 from simulation results of other models without verifi-  
 470 cation of the models’ internal consistency. Energy con-  
 471 servation, for example, is one of the key principles to  
 472 ensure, and this both with respect to directional (BRFs)  
 473 and hemispherically integrated (fluxes) quantities.

#### 3.1.1. Energy conservation

476 The solar radiation entering a plant canopy is parti-  
 477 tioned into an absorbed  $A$ , a reflected  $R$  and a trans-  
 478 mitted  $T$  fraction such that all incident photons are  
 479 accounted for. Energy conservation thus requires that  
 480  $A + R + (1 - \alpha)T = 1$ , where  $\alpha$  is the soil brightness. The  
 481 capacity of a given model ( $m$ ) to conserve energy can be  
 482 described using:

$$\Delta_F(m) = \frac{1}{N_F(m)} \sum_{\lambda=1}^{N_\lambda^m} \sum_{\zeta=1}^{N_\zeta^m} \sum_{i=1}^{N_{\Omega_i}^m} \left[ A_m(\lambda, \zeta, i) + R_m(\lambda, \zeta, i) \right]$$

$$+[1 - \alpha(\lambda)] T_m(\lambda, \zeta, i) \Big] - 1$$

483 where  $N_F(m) = N_\lambda^m + N_\zeta^m + N_{\Omega_i}^m$  is the total number  
 484 of spectral  $\lambda$ , structural  $\zeta$ , and illumination  $\Omega_i$  condi-  
 485 tions for which flux simulations were performed by model  
 486  $m$ . Figure 2 shows the mean deviation from energy con-  
 487 servation,  $\Delta_F(m)$  for those models that simulated flux  
 488 quantities in the case of the structurally homogeneous  
 489 baseline scenarios. More specifically, the top panel dis-  
 490 plays  $\Delta_F(m)$  for canopies with discrete leaves in the solar  
 491 domain, and the bottom panel shows  $\Delta_F(m)$  for turbid  
 492 medium canopies with conservative scattering properties  
 493 (purist corner). It should be noted that the **MAC** model  
 494 seems to generate an excess of energy ( $\Delta_F(\text{MAC}) > 0$ )  
 495 that is equivalent to about 3% of the incident radiation  
 496 at the TOC in the solar domain. On the other hand,  
 497 the **FLIGHT** and **raytran** models both appear to lose en-  
 498 ergy ( $\Delta_F < 0$ ), equivalent to  $\sim 2\%$  of the incident radi-  
 499 ation at those wavelengths. Under conservative scattering  
 500 conditions, however, the latter two models comply very  
 501 well with energy conservation requirements ( $\Delta_F \approx 0$ ),  
 502 a pattern that is observed for both discrete and turbid  
 503 medium foliage representations in structurally ho-  
 504 mogeneous, as well as heterogeneous environments (not  
 505 shown). Since  $\alpha = 1$  under purist corner conditions it  
 506 must be the canopy transmission measurement that af-  
 507 fects  $\Delta_F$  for both **FLIGHT** and **raytran**. Indeed, in the  
 508 case of **raytran** it turned out that the diffuse transmis-  
 509 sion component had been neglected in the submitted  
 510 simulations. By the same token the deviations of the  
 511 **DART** model under conservative scattering conditions are  
 512 likely to arise from its estimation of the canopy absorp-  
 513 tion and/or reflectance. Further analysis (not shown)  
 514 indicated that enhanced multiple scattering conditions  
 515 exacerbate the apparent deviations from energy conser-  
 516 vation for all models with non-zero  $\Delta_F$  values in Figure 2.  
 517 As to how much these apparent deviations from energy  
 518 conservation relate to model deficiencies rather than op-  
 519 erator errors is, however, difficult to anticipate. By the  
 520 same token, RT models that utilise the principle of en-  
 521 ergy conservation to close their radiation budget will ob-  
 522 viously never be found deviating in such self-consistency  
 523 checks. This applies, for example, to the **1/2-discret**,  
 524 **Sail++** and **2-Stream** models which derive their canopy  
 525 absorption estimate from simulations of the reflectance  
 526 and transmission properties of the vegetation layer.  
 527

### 528 3.1.2. BRF consistency

529 The RAMI format specifications ask for all radiative  
 530 quantities to be provided with a precision of six decimal  
 531 places, *i.e.*, the implicit error associated with the mea-  
 532 surements is thus of the order of  $10^{-6}$ . The average ab-  
 533 solute difference  $\Delta\rho$  between the total BRF ( $\rho_{tot}$ ) and the  
 534 sum of the BRF contributions due to the single uncollided  
 535 ( $\rho_{uc}$ ), the single-collided ( $\rho_{co}$ ), and the multiple-collided  
 536 ( $\rho_{mt}$ ) radiation components should thus be of a similar  
 537 magnitude when defined as follows:

$$\begin{aligned}
 \Delta\rho(m) = & \frac{1}{N_\rho(m)} \sum_{\lambda=1}^{N_\lambda^m} \sum_{\zeta=1}^{N_\zeta^m} \sum_{v=1}^{N_{\Omega_v}^m} \sum_{i=1}^{N_{\Omega_i}^m} \left| \rho_{tot}^m(\lambda, \zeta, v, i) \right. \\
 & \left. - [\rho_{uc}^m(\lambda, \zeta, v, i) + \rho_{co}^m(\lambda, \zeta, v, i) + \rho_{mt}^m(\lambda, \zeta, v, i)] \right|
 \end{aligned}$$

538 where  $N_\rho(m) = N_\lambda^m + N_\zeta^m + N_{\Omega_v}^m + N_{\Omega_i}^m$  is the total  
 539 number of BRFs that were generated with the model  $m$

540 for different spectral  $\lambda$ , structural  $\zeta$ , viewing  $\Omega_v$ , and  
541 illumination  $\Omega_i$  conditions. Apart from **Hyemalis** and  
542 **2-Stream**, all models in Table 1 provided simulations of  
543 the three BRF components for at least some of the test  
544 cases of RAMI-3. In general, the average absolute deviation  
545  $\Delta\rho$  was  $< 10^{-5}$ , with the exception of  $\Delta\rho(\mathbf{5Scale}) =$   
546  $0.0027$  for the discrete homogeneous solar domain, as well  
547 as  $\Delta\rho(\mathbf{frat}) = 0.0013$  and  $\Delta\rho(\mathbf{FLIGHT}) = 0.0002$  for the  
548 homogeneous discrete purist corner. These deviations,  
549 although small in terms of the magnitude of the total  
550 BRF and often related to the configuration of the model  
551 in its day to day usage, are nevertheless significant in the  
552 context of a model intercomparison exercise like RAMI  
553 since—by their statistical nature—they seem to indicate  
554 that some of the models do not conserve energy when  
555 partitioning the total BRF into its various subcomponents.  
556

### 557 3.1.3. Spectral ratio of the single-uncollided BRF

559 Model self-consistency can also be evaluated across  
560 different wavelengths. The ratio  $\rho_{uc}(\lambda_1)/\rho_{uc}(\lambda_2)$  of the  
561 single-uncollided BRF components in the red and NIR  
562 spectral regimes, for example, relates to the differing  
563 amounts of radiation that have been scattered once by  
564 the underlying background (and never interacted with  
565 the canopy foliage) at these two wavelengths ( $\lambda_1$  and  $\lambda_2$ ).  
566 In the case of Lambertian soils, this spectral ratio must  
567 be a directionally invariant constant equal to the ratio  
568 of the soil albedos at the wavelengths of interest, *i.e.*,  
569  $\alpha(\lambda_1)/\alpha(\lambda_2)$ . Ensemble-averaging over a variety of structure  
570  $\zeta$  and illumination  $\Omega_i$  conditions ( $N_S = N_\zeta^m + N_{\Omega_i}^m$ )  
571 then provides an indication of the average deviation from  
572 spectral consistency for any model  $m$ :

$$\Delta_S(m, \Omega_v) = \frac{\alpha(\lambda_1)}{\alpha(\lambda_2)} - \left[ \frac{1}{N_S(m)} \sum_{\zeta=1}^{N_\zeta^m} \sum_{i=1}^{N_{\Omega_i}^m} \frac{\rho_{uc}^m(\lambda_1, \zeta, \Omega_v, i)}{\rho_{uc}^m(\lambda_2, \zeta, \Omega_v, i)} \right]$$

573 Figure 3 documents the angular variation of  $\Delta_S$ , obtained  
574 from single-uncollided BRF simulations in the red and  
575 NIR spectral domains, for homogeneous turbid medium  
576 (left) and discrete floating-spheres canopies (right) hav-  
577 ing uniform LNDs. Not included in these graphs are  
578 the forward MC ray-tracing models **frat** and **raytran**  
579 due to the large noise levels associated with their sam-  
580 pling schemes. MC noise is also evident for the **drat** and  
581 **Rayspread** models, although this decreases as more rays  
582 are being used in the RT simulation and/or the fraction  
583 of the contributing background in the scene increases,  
584 *e.g.*, in the “floating spheres” scenarios. One will notice  
585 that, with the exception of the **Sprint3** model in the  
586 “floating spheres” case, the spectral ratio of the single-  
587 uncollided BRF component remains relatively constant  
588 for all models (including **ACRM** in the homogeneous dis-  
589 crete case – not shown) up to view zenith angles of about  
590  $65 - 70^\circ$ . The **Sprint3** model, and to a lesser extent  
591 also the **Rayspread** model, utilise a variance reduction  
592 technique known as “photon spreading” in order to re-  
593 duce the number of rays that sample the radiative trans-  
594 fer properties of the medium of interest. In Figure 3  
595 the deviations in the magnitude but not in the shape  
596 of the single-uncollided BRF components in the homo-  
597 geneous turbid case (left panel) may thus be solely due  
598 to an insufficient sampling (LAI=3) of the lower bound-  
599 ary condition contributing to  $\rho_{uc}$ . On the other hand,  
600 the variations of  $\Delta_S(\mathbf{Sprint3})$  with view zenith angle in  
601 the “floating spheres” case (LAI=2.36) may be due to

602 the spatially varying presence of foliage in the canopy to-  
 603 gether with the statistical distribution of foliage—rather  
 604 than a deterministic placement of scatterers—within the  
 605 various spherical volumes. As such the actual number  
 606 of rays, that traverse the floating spheres (LAI=5) and  
 607 reach the ground or escape the scene unhindered, is never  
 608 the same in different directions if model runs at different  
 609 wavelengths do not use the same starting seeds to ini-  
 610 tialise their random number generator.

### 3.2. Absolute model performance

611 Exact analytical solutions to the radiative transfer  
 612 equation do not exist for the vast majority of conceiv-  
 613 able vegetation canopies. In some cases, however, the  
 614 structural and spectral properties of vegetated surfaces  
 615 may be such that it becomes possible to predict at least  
 616 some of their radiative properties analytically. Within  
 617 the available set of RAMI test cases there are at least two  
 618 different types of absolute model evaluations that can be  
 619 performed: The first one relates to single-collided BRF  
 620 components of structurally homogeneous turbid medium  
 621 canopies with uniform LND, and the second to the re-  
 622 flected and absorbed energy fluxes in the various conser-  
 623 vative scattering (purist corner) scenarios.

624

#### 3.2.1. Homogeneous turbid uniform canopy

625 Structurally homogeneous leaf canopies with az-  
 626 imuthally invariant uniform LNDs are characterised by  
 627 a constant probability of foliage interception irrespective  
 628 of the direction of propagation in that medium [Ross,  
 629 1981; Verstraete, 1987]. In addition, turbid media—with  
 630 their infinitesimally small scatterers—satisfy the far field  
 631 approximation and thus never yield a hot spot, *i.e.*, a  
 632 localised increase in the BRF around the retro-reflection  
 633 direction of the incident illumination, *e.g.*, Gerstl [1988];  
 634 Verstraete [1988]; Kuusk [1991]. The single-uncollided  
 635 BRF component of such a canopy can be written as:  
 636

$$\rho_{uc}(\Omega_i, \Omega_v) = \alpha \exp \left[ \frac{-\text{LAI}(\mu_i + \mu_v)}{2\mu_i\mu_v} \right]$$

637 where  $\alpha$  is the albedo of the Lambertian soil,  $\mu = \cos \theta$   
 638 is the cosine of the illumination ( $i$ ) or view ( $v$ ) zenith  
 639 angle  $0 \leq \theta \leq \pi/2$ , and LAI is the leaf area index of the  
 640 canopy. Similarly the single-collided BRF component of  
 641 such a canopy can be written as:

$$\rho_{co}(\Omega_i, \Omega_v) = \frac{2\Gamma(\Omega_i \rightarrow \Omega_v) \left[ 1 - \exp \frac{-\text{LAI}(\mu_i + \mu_v)}{2\mu_i\mu_v} \right]}{\mu_i + \mu_v}$$

642 where the canopy scattering phase function is given by  
 643 [Shultis and Myneni, 1988]:

$$\Gamma(\Omega_i \rightarrow \Omega_v) = \frac{r_L + t_L}{3\pi} (\sin \beta - \beta \cos \beta) + \frac{t_L}{3} \cos \beta$$

644 and  $\beta$  is the phase angle between the illumination and  
 645 viewing direction:

$$\cos \beta = \cos \theta_i \cos \theta_v + \sin \theta_i \sin \theta_v \cos |\phi_i - \phi_v|$$

646 and  $r_L$  ( $t_L$ ) is the reflectance (transmittance) of the fo-  
 647 liage elements. Figure 4 shows the mean absolute error  
 648 between RT model simulations and the above analyti-  
 649 cal formulations for the single-collided (left panel) and  
 650 the single-uncollided (right panel) BRF components of

651 a turbid medium canopy with uniform LND and Lam-  
652 bertian scattering laws. The averaging was performed  
653 over BRF simulations in the principal and orthogonal  
654 planes, as well as, for illumination zenith angles of  $20^\circ$   
655 and  $50^\circ$ . With the exception of **MBRF** all RT models lie  
656 within 0.0025 of the truth in the single-collided case. The  
657 operator of the **MBRF** model conjectures, however, that  
658 the observed deviations may be due to a software error  
659 (bug) since the formulation of the single-collided BRF  
660 component in *Qin and Xiang* [1997] is based on a proper  
661 theoretical derivation. In the single-uncollided case the  
662 agreement between the participating RT models and the  
663 analytical solution is ten times better still than in the  
664 single-collided case, *i.e.*, all models lie within  $2.5 \cdot 10^{-4}$   
665 of the analytical solutions. This is impressive since the  
666 magnitude of  $\rho_{co}$  ( $\rho_{uc}$ ) along the orthogonal plane was  
667 typically around 0.017 (0.003) in the red and 0.16 (0.005)  
668 in the NIR. Furthermore, it should be noted that none of  
669 the participants had any *a priori* knowledge about these  
670 absolute evaluation tests. In principle, the performance  
671 of many of the participating RT models could thus still be  
672 improved further, for example, by increasing the number  
673 of integration steps (*e.g.*, Gaussian quadrature points)  
674 in numerical techniques, or, by adding further rays to  
675 sample the characteristics of the canopy-leaving radia-  
676 tion field (in the case of MC ray-tracing models).

677

### 678 3.2.2. Purist corner fluxes

679 Under conservative scattering conditions all of the en-  
680 ergy that enters a canopy system has to leave it, *i.e.*,  
681  $R = 1$  and  $A = 0$ . The RAMI purist corner thus pro-  
682 vides another opportunity to assess the performance of  
683 RT models against a known absolute reference. Figure 5  
684 shows (on a log-log scale) the average absolute deviation  $\varepsilon$   
685 from the true canopy absorption (y-axis) and reflectance  
686 (x-axis) for homogeneous canopies with finite-sized (left  
687 panel), as well as turbid medium (right panel) foliage rep-  
688 resentations under conservative scattering properties. In  
689 each case the averaging was performed over ( $N = 18$ ) test  
690 cases with different LAI, LND and  $\theta_i$ . With the excep-  
691 tion of **MBRF**, which did not provide absorption estimates,  
692 all models featuring  $\varepsilon = 10^{-7}$  (or -7 in Figure 5) sub-  
693 mitted the theoretical values. In the homogeneous turbid  
694 case, for example, both the **raytran**, and **Sprint3** models  
695 compute the canopy absorption and reflectance to within  
696 computer-precision uncertainties. The **1/2-discret** and  
697 **2-Stream** models, on the other hand, showed an aver-  
698 age absolute deviation of 0.0015 and 0.0245, respectively,  
699 for both  $\varepsilon_{\text{Absorption}}$  and  $\varepsilon_{\text{Reflectance}}$ . Models that fall on  
700 the 1:1 line in Figure 5 estimate their canopy absorp-  
701 tion by closing the energy budget. In the case of the  
702 **1/2-discret** model the (negative) canopy absorption de-  
703 viations arose from overestimated albedos under the fully  
704 scattering purist corner conditions. These in turn, are a  
705 consequence of the fixed number (16) of Gaussian quadra-  
706 ture points used in the numerical integration scheme of  
707 the azimuthally averaged multiple-scattering component.  
708 The **DART** model, on the other hand, which computes  
709 canopy absorption on a ray-by-ray basis, features a re-  
710 spectable  $\varepsilon_{\text{Absorption}} = 0.0006$  and  $\varepsilon_{\text{Reflectance}} = 0.0125$ .  
711 In the discrete homogeneous case (right panel), the av-  
712 erage absolute deviation of the **1/2-discret** model from  
713 the correct absorption and reflectance values increases to  
714 0.0204, presumably due to highly variable BRFs in the  
715 vicinity of the retro-reflection direction (hot spot) that af-  
716 fected the accuracy of the numerical integration scheme.  
717 At this point, one should recall that the lack of deviations  
718 from the “truth” is not a proof of the physical correctness

719 of a model since, for example, hard-encoded program-  
 720 ming statements may be contained inside the computer  
 721 code that do account for the eventuality of situations for  
 722 which the exact solution is known. In this way, the ac-  
 723 tual model would not be executed—to compute canopy  
 724 reflectance and absorption here—but sidestepped to gener-  
 725 ate the anticipated results. The primary interest here  
 726 (and in all other parts of section 3) thus lies in under-  
 727 standing the observed *deviations* from the correct solu-  
 728 tion.

### 3.3. Relative model performance

729 Without access to absolute reference standards the  
 730 evaluation of RT models has to rely on relative model  
 731 intercomparison. The goal being to identify systematic  
 732 trends in the behaviour of one (or more) models with  
 733 respect to others, over ensembles of test cases. Three  
 734 different types of relative intercomparison metrics will  
 735 be proposed here: model-to-model deviations, model-to-  
 736 ensemble deviations, and deviations from model-derived  
 737 surrogate truths.

#### 3.3.1. Model-to-model deviations

740 The differences in the BRF simulations between two  
 741 models ( $c$  and  $m$ ), when averaged over a variety of spec-  
 742 tral ( $\lambda$ ), structural ( $\zeta$ ), viewing ( $\Omega_v$ ) and illumination  
 743 ( $\Omega_i$ ) conditions, can be defined as:

$$\delta_{m \leftrightarrow c} = \frac{200}{N} \sum_{\lambda=1}^{N_\lambda} \sum_{\zeta=1}^{N_\zeta} \sum_{v=1}^{N_{\Omega_v}} \sum_{i=1}^{N_{\Omega_i}} \left| \frac{\rho_m(\lambda, \zeta, v, i) - \rho_c(\lambda, \zeta, v, i)}{\rho_m(\lambda, \zeta, v, i) + \rho_c(\lambda, \zeta, v, i)} \right|$$

744 where  $N = N_\lambda + N_\zeta + N_{\Omega_v} + N_{\Omega_i}$  is the total number  
 745 of BRF simulations that have been performed by both  
 746 models  $c$  and  $m$ , and  $\delta_{m \leftrightarrow c}$  is expressed in percent.

747 Figure 6 depicts a series of two-dimensional grids con-  
 748 taining information on the various model-to-model BRF  
 749 differences (blue-red colour scheme in the lower right half  
 750 of each panel), as well as, the percentage of the total  
 751 number of BRFs over which the  $\delta_{m \leftrightarrow c}$  values were de-  
 752 rived (black-green colour scheme in upper left half of each  
 753 panel). More specifically,  $\delta_{m \leftrightarrow c}$  is shown for those models  
 754 having submitted the total (top row), single-uncollided  
 755 (second row), single-collided (third row) and multiple-  
 756 collided (bottom row) BRF data for structurally homo-  
 757 geneous canopies with finite-sized (leftmost column) and  
 758 turbid medium (middle-left column) foliage representa-  
 759 tions, as well as, for “floating spheres” scenarios with  
 760 finite-sized (middle-right column) and turbid medium  
 761 (rightmost column) foliage representations in the solar  
 762 domain. The blue colour scale increments in steps of  
 763 2%, the green colour scale in steps of 10%, and the red  
 764 also in steps of 10% with the bright red colour indicat-  
 765 ing values larger than 50%. The maximum number of  
 766 BRF simulations included in the computation of  $\delta_{m \leftrightarrow c}$   
 767 was 1216 for the structurally homogeneous and 608 for  
 768 the “floating spheres” canopies. To illustrate the reading  
 769 of the various panels in Figure 6 let’s consider, for exam-  
 770 ple, the total BRFs of the **Hyemalis** and **Sprint3** models  
 771 in the discrete homogeneous case (top left panel): Their  
 772 model-to-model difference value, which lies between 10  
 773 and 20% (light red colour), has been obtained from less  
 774 than 10% of the total number of BRF simulations (dark  
 775 green colour) and thus may not be too representative.  
 776 On the other hand, the  $\delta_{m \leftrightarrow c}$  of the **ACRM** and **Sprint3**  
 777 models (same top left panel) lies somewhere between 6  
 778 and 8% and has been established using 100% of the pos-

779 sible BRFs. In general, the majority of models in the  
780 discrete and turbid homogeneous cases agree rather well  
781 with each other ( $\delta_{m \leftrightarrow c} < 10\%$ ). This behaviour is also  
782 present for the various BRF components with the ex-  
783 ception of the single-uncollided BRF component ( $\rho_{uc}$ ) in  
784 the discrete homogeneous case where the various imple-  
785 mentations/approximations of the hot spot phenomenon  
786 have increased the differences amid the simulated BRFs.  
787 In the case of turbid homogeneous canopies the DART  
788 model features somewhat elevated  $\delta_{m \leftrightarrow c}$  values for the  
789  $\rho_{uc}$  component which may, however, be partly due to  
790 the inter/extrapolation procedure that had to be sys-  
791 tematically applied to all BRF simulations of this model  
792 in order to map its submitted 32 (18) viewing condi-  
793 tions in the principal (orthogonal) plane to the full set  
794 of 76 as specified by RAMI. The FLIGHT model—which  
795 did not update its baseline scenario simulations during  
796 RAMI-3—shows slightly diverging multiple-collided BRF  
797 components in both the discrete and turbid medium ho-  
798 mogeneous cases. These are caused by a Lambertian  
799 assumption governing the angular distribution of higher  
800 orders of scattered radiation in simulation results origi-  
801 nally submitted during RAMI-1. This effect is no longer  
802 visible in the “floating spheres” case due to subsequent  
803 model improvements in phase 2 (right panels in Fig-  
804 ure 6). Unlike in the discrete homogeneous cases, the  
805 “floating spheres”  $\rho_{uc}$  shows the smallest  $\delta_{m \leftrightarrow c}$  values  
806 presumably because the hotspot here is dominated by  
807 the geometry of the spheres themselves. In the “float-  
808 ing spheres” cases it is thus the multiple scattering and  
809 to a lesser extent also the single-collided BRF compo-  
810 nents that show the largest differences between BRF sim-  
811 ulations of 3-D Monte Carlo models—featuring explicit  
812 scene representations—and those of somewhat more ap-  
813 proximate models.

814

### 815 3.3.2. Model-to-ensemble deviations

816 In the absence of any absolute reference truth, the out-  
817 put from individual RT models may also be compared  
818 to ensemble averages computed from simulation results  
819 of other RT models, as first proposed by *Pinty et al.*  
820 [2001, 2004b]. In this way, RT models that are very differ-  
821 ent from all other models can be identified and—although  
822 not wrong in any absolute sense—they may then be ex-  
823 cluded from further iterations of the ensemble averaging  
824 process, if this is deemed appropriate. For any spectral  
825 ( $\lambda$ ), structural ( $\zeta$ ), viewing ( $v$ ), and illumination ( $i$ ) con-  
826 dition one can compute:

$$\delta_m(\lambda, \zeta, v, i) = \frac{200}{N_c} \sum_{c=1; c \neq m}^{N_c} \left| \frac{\rho_m(\lambda, \zeta, v, i) - \rho_c(\lambda, \zeta, v, i)}{\rho_m(\lambda, \zeta, v, i) + \rho_c(\lambda, \zeta, v, i)} \right|$$

827 where  $N_c$  is the number of models with which the output  
828 of model  $m$  is to be compared. One way to analyse such  
829  $\delta_m$  statistics is to bin them over a variety of conditions  
830 in order to yield a histogram of model-to-ensemble de-  
831 viations. The inlaid graphs in Figure 7 show a variety  
832 of  $\delta_m$  histograms generated from total BRF simulations  
833 of the 1/2-discret, drat, FLIGHT, frat, Rayspread,  
834 raytran, RGM, Sail++, Sprint3, and 4SAIL2 models in the  
835 case of the discrete structurally homogeneous canopies  
836 (left panel), and the drat, FLIGHT, Rayspread, raytran,  
837 and Sprint3 models in the case of the discrete “float-  
838 ing spheres” canopies (right panel). The main graphs  
839 of Figure 7 show the outer envelope of these  $\delta_m$  his-  
840 tograms both for the discrete structurally homogeneous  
841 canopies (left panel) and the discrete “floating spheres”

842 canopies (right panel). One will notice that the agree-  
 843 ment between the RT models in RAMI-3 (red line) is  
 844 better than the corresponding agreement of models dur-  
 845 ing the previous phase of RAMI three years ago (black  
 846 line). In the homogeneous baseline scenarios, where more  
 847 models are included than during RAMI-2, the first peak  
 848 of the histogram envelope ( $0 \leq \delta_m \leq 2.5\%$ ) can be  
 849 attributed primarily to the models `1/2-discret`, `drat`,  
 850 `FLIGHT`, `Rayspread` and `raytran`. The second half of the  
 851 histogram envelope ( $\delta_m > 2.5\%$ ), on the other hand,  
 852 arises from BRF simulations due to the models `frat`,  
 853 `MAC`, `RGM`. The models `Sail++` and `Sprint3`—with their  
 854 broader distributions of  $\delta_m$ —contribute to both parts of  
 855 the histogram envelope.

856  
 857 Alternatively one may define an overall indicator of  
 858 model-to-ensemble differences,  $\bar{\delta}_m$  [%] by averaging the  
 859 above  $\delta_m(\lambda, \zeta, v, i)$  over appropriate sets ( $\bar{N}$ ) of spectral  
 860  $\lambda$ , structural  $\zeta$ , viewing  $v$  and illumination  $i$  conditions:

$$\bar{\delta}_m = \frac{1}{\bar{N}} \sum_{\lambda=1}^{N_\lambda} \sum_{\zeta=1}^{N_\zeta} \sum_{v=1}^{N_{\Omega_v}} \sum_{i=1}^{N_{\Omega_i}} \delta_m(\lambda, \zeta, v, i)$$

861 Table 2 shows the values of the overall model disper-  
 862 sion indicator  $\bar{\delta}_m$  [%] obtained from an ensemble of six  
 863 3-D Monte Carlo models, namely: `DART`, `drat`, `FLIGHT`,  
 864 `Rayspread`, `raytran` and `Sprint3`. For each one of these  
 865 models  $\bar{\delta}_m$  is provided for the total BRF ( $\rho_{tot}$ ) as well as  
 866 the single-collided ( $\rho_{co}$ ), the multiple-collided ( $\rho_{mt}$ ), and  
 867 the single-uncollided ( $\rho_{uc}$ ) BRF components using sub-  
 868 mitted simulation results from either RAMI-2 or RAMI-  
 869 3. With the exception of the total BRF simulations of  
 870 `DART` all other  $\bar{\delta}_m$  values improved between RAMI-2 and  
 871 RAMI-3, meaning that a smaller dispersion exists be-  
 872 tween the BRF values of the latest version of these mod-  
 873 els. The average dispersion between the total BRF sim-  
 874 ulations of the six 3-D MC models was found to have  
 875 almost halved from RAMI-2 (1.37 %) to RAMI-3 (0.72  
 876 %) in the discrete case, and in the turbid medium case  
 877 it improved by a factor of  $\sim 7$  from RAMI-2 (6.36 %) to  
 878 RAMI-3 (0.91 %).

### 879 3.3.3. Model-to-surrogate-truth deviations

881 Monte Carlo RT models allow for explicit 3-D repre-  
 882 sentations of complex canopy architectures by describing  
 883 these environments with (sometimes Boolean combina-  
 884 tions of) sufficiently small geometric building blocks of  
 885 known radiative properties. Solving the radiative trans-  
 886 fer equation for such 3-D environments is then achieved  
 887 through a stochastic sampling of the surface-leaving ra-  
 888 diation field [Disney et al., 2000]. Since this is a time  
 889 consuming undertaking—in particular for complex 3-D  
 890 scenes—the current generation of 3-D MC models dif-  
 891 fer primarily in the amount of deterministic detail that is  
 892 used when constructing a scene, and, in the approach and  
 893 extent to which ray trajectories are sampled within the  
 894 3-D media. Both Figure 6 and Table 2 indicate that the  
 895 3-D Monte Carlo models, `DART`, `drat`, `FLIGHT`, `Rayspread`,  
 896 `raytran` and `Sprint3` are generally in very close agree-  
 897 ment with each other. In particular the numbers in Ta-  
 898 ble 2 support their usage in attempts to provide a “sur-  
 899rogate truth” estimate against which further RT model  
 900 comparisons may then be carried out. One simple way to  
 901 obtain a “surrogate truth” estimate is by averaging the  
 902 BRFs obtained from a set of  $N_{3D}^{credible}$  credible 3-D MC  
 903 models, that is:

$$\bar{\rho}_{3D}(\lambda, \zeta, v, i) = \frac{1}{N_{3D}^{credible}} \sum_{n=1}^{N_{3D}^{credible}} \rho_{3D}(\lambda, \zeta, v, i; n)$$

904 where the precise number and names of the 3-D MC mod-  
 905 els that feature within  $N_{3D}^{credible}$  is selected from among  
 906 the following models: **DART**, **drat**, **FLIGHT**, **Rayspread**,  
 907 **raytran** and **Sprint3**. The selection procedure is ap-  
 908 plied to every RAMI experiment and measurement type  
 909 individually and adheres to the following list of criteria:

- 910
- 911 • For every RAMI BRF (flux) measurement, identify  
 912 at least two (one) 3-D Monte Carlo models that do not  
 913 belong to the same RT modelling school/family,
- 914 • If two models from the same RT modelling  
 915 school/family are available, *e.g.*, **Rayspread** and **raytran**,  
 916 choose the one with the least amount of apparent MC  
 917 noise,
- 918 • Remove all those 3-D Monte Carlo models from the  
 919 reference set that are noticeably different from the main  
 920 cluster of 3-D MC simulations,
- 921 • If sufficient models are contained in the main cluster  
 922 of 3-D MC simulations then remove those models that  
 923 would introduce noticeable levels of “MC noise” into the  
 924 reference set,
- 925 • If there are two distinct clusters of 3-D Monte Carlo  
 926 models, or, no obvious cluster at all, then use all avail-  
 927 able 3-D RT models to define a reference solution.

928  
 929 A synoptic table featuring the names of the various  
 930 3-D MC models that contribute toward the computa-  
 931 tion of  $\bar{\rho}_{3D}$  for all the RAMI-3 experiments and mea-  
 932 surement types individually, can be found on the fol-  
 933 lowing internet page: [http://romc.jrc.it/WWW/PAGES/ROMC\\_Home/RAMIREF.html](http://romc.jrc.it/WWW/PAGES/ROMC_Home/RAMIREF.html)<sup>3</sup>.

934  
 935  
 936 Once the “surrogate truth” is available for the various  
 937 RAMI baseline scenarios, the deviations of individual RT  
 938 models from this norm may be quantified with the fol-  
 939 lowing metric [Pinty *et al.*, 2004b]:

$$\chi_m^2(\lambda) = \frac{1}{N-1} \sum_{\zeta=1}^{N_\zeta} \sum_{v=1}^{N_{\theta_v}} \sum_{i=1}^{N_{\theta_i}} \frac{[\rho_m(\lambda, \zeta, v, i) - \bar{\rho}_{3D}(\lambda, \zeta, v, i)]^2}{\sigma^2(\lambda, \zeta, v, i)}$$

940 where  $\sigma(\lambda, \zeta, v, i) = f \cdot \bar{\rho}_{3D}(\lambda, \zeta, v, i)$  corresponds to a  
 941 fraction  $f$  of the average BRF obtained from the credible  
 942 3-D Monte Carlo models.

943 Figure 8 displays the  $\chi^2$  values in the red and NIR  
 944 wavelengths for the structurally homogeneous (left panel)  
 945 and the “floating spheres” (right panel) baseline scenarios  
 946 having finite-sized scatterers. Arrows indicate changes  
 947 in the  $\chi^2$  values when comparing the performance of a  
 948 model in RAMI-2 (base of arrow) with that in RAMI-  
 949 3 (tip of arrow) using the latter  $\bar{\rho}_{3D}$  as reference. The  
 950 uncertainty in both the model and surrogate truth was  
 951 set to 3% of the latter, *i.e.*,  $f = 0.03$ . This estimate  
 952 is in line with the absolute calibration accuracy of cur-  
 953 rent space borne instruments like MISR [Bruegge *et al.*,  
 954 2002] and MERIS [Kneubühler *et al.*, 2002], among oth-  
 955 ers. Obviously there is a tendency for those 3-D MC mod-  
 956 els that have participated in the computation of  $\bar{\rho}_{3D}$  to  
 957 have smaller  $\chi^2$  values in RAMI-3 than in RAMI-2. This  
 958 is particularly so for the heterogeneous BRF simulations,  
 959 where **drat**, **FLIGHT**, **Rayspread** and **sprint-3** served as  
 960 credible models for all the “floating spheres” test cases.

961 In the homogeneous case, however, both the number and  
962 names of the credible 3-D MC models changed from one  
963 test case to another. RT models that did not update  
964 their BRF simulations in any significant manner during  
965 RAMI-3, *e.g.*, `1/2-discret` and `FLIGHT`, do not show any  
966 dynamics in their  $\chi^2$  values in the depicted graphs. Oth-  
967 ers, like the `Sail++` and `RGM` models in the homogeneous  
968 case, for example, have reduced the distance between  
969 their BRF simulations and  $\bar{\rho}_{3D}$  in RAMI-3 which trans-  
970 lates into smaller  $\chi^2(\text{red})$  and  $\chi^2(\text{NIR})$  values when com-  
971 pared to those of RAMI-2. `FRT` was the only non Monte  
972 Carlo model to participate in the “floating spheres” test  
973 cases during both RAMI-2 and RAMI-3. Here one notices  
974 a substantial improvement in its  $\chi^2(\text{NIR})$  value together  
975 with a slight increase in  $\chi^2(\text{red})$ .

## 4. New test cases in RAMI-3

976 A series of additional experiments and measurements  
977 were proposed for RAMI-3 that address new issues or  
978 complement others raised during RAMI-2. In the follow-  
979 ing, the results obtained for the “birch stand” canopy will  
980 be presented first. Next the “true zoom-in” scene, with  
981 its additional measurements, will be revisited before com-  
982 paring the BRF simulation results for the “conifer forest”  
983 scene with and without topography. Last but not least,  
984 results for the “floating spheres” purist corner will also  
985 be displayed.

### 4.1. The birch stand

986 This set of experiments was suggested to simulate the  
987 radiative transfer regime in the red and near-infrared  
988 spectral bands for spatially heterogeneous scenes resem-  
989 bling boreal birch stands (see Figure 9). The  $100 \times 100 \text{ m}^2$   
990 scene is composed of a large number of non-overlapping  
991 tree-like entities of different sizes and spectral proper-  
992 ties that are randomly located across (and only partially  
993 covering) a planar surface representing the underlying  
994 background. Individual tree objects were represented  
995 by an ellipsoidal crown located just above a cylindrical  
996 trunk. The finite sized foliage was randomly distributed  
997 within the ellipsoidal volumes that represented the tree  
998 crowns, and was characterized by radiative properties (re-  
999 flectance, transmittance) that are typical for birch trees.  
1000 Table 3 provides an overview of the structural and spec-  
1001 tral properties associated with the 5 tree classes of the  
1002 “birch stand” scene.

1003

1004

#### 4.1.1. Canopy-level BRF simulations

1005 Figure 10 presents model generated total BRFs in the  
1006 red (left column) and NIR (right column) spectral do-  
1007 main corresponding to observations of the “birch stand”  
1008 along the principal (upper panels) and orthogonal (lower  
1009 panels) planes for illumination conditions of  $\theta_i = 20^\circ$  and  
1010  $\theta_i = 50^\circ$ . It can be seen that most models generate rela-  
1011 tively similar BRF patterns with the exception of `5Scale`.  
1012 This systematic difference may be partly explained by  
1013 the fact that `5Scale` implemented a “birch stand” scene  
1014 composed of only one single tree class having structural  
1015 and spectral properties that corresponded to the aver-  
1016 age characteristics of the 5 tree classes described on the  
1017 RAMI website. Moreover, `5Scale`’s multiple scattering  
1018 scheme was designed for denser forests than the “birch  
1019 stand” scene with a mean LAI of 0.398. The `drat` model  
1020 generates BRFs that, in particular in the red spectral do-  
1021 main, have a tendency to be somewhat higher than those  
1022 of `Dart`, `Rayspread`, `raytran` and `Sprint3`. Further anal-  
1023 ysis revealed that these differences arise primarily due

1024 to the single-collided foliage BRF component. One possible  
1025 explanation may be found in the exact spatial ar-  
1026 rangement of the various discrete leaf elements that make  
1027 up the crown foliage in the `drat` simulations. The com-  
1028 monly used procedure of “cloning” individual tree objects  
1029 when generating a larger canopy scene, may imply that  
1030 small differences in the leaf orientations and positions—  
1031 especially along the rim of the crown volume—translate  
1032 into noticeable differences in the simulated BRF values  
1033 at the level of the whole scene. These differences are,  
1034 however, only detectable due to the increasing agree-  
1035 ment that now exists between the various RT models that  
1036 have contributed to RAMI-3. The histograms of model-  
1037 to-ensemble BRF differences,  $\delta_m$  in the “birch stand”  
1038 scene (central panels in Figure 10), for example, show  
1039 that the BRFs simulated by any one of the models `Dart`,  
1040 `drat`, `frrt`, `Rayspread`, `raytran` and `Sprint3` typically fall  
1041 within 2% of the ensemble average—and this irrespective  
1042 of the plane of observation.

1043

#### 1044 4.1.2. Local transmission transects

1045 Since the  $x, y$  location of every individual tree in the  
1046 “birch stand” scene was specified on the RAMI website  
1047 a new measurement type—asking for local transmission  
1048 measurements along a transect of 21 adjacent  $1 \times 1 \text{ m}^2$   
1049 patches—had been proposed. Models were asked to pro-  
1050 vide simulation results quantifying the total (*i.e.*, direct  
1051 plus diffuse) transmission of radiation at the level of the  
1052 background for two transects located at the center of the  
1053 birch stand scene with orientations that were parallel and  
1054 perpendicular to the azimuthal direction of the incident  
1055 radiation,  $\phi_i$ , respectively. This setup, which aimed at  
1056 reproducing conditions resembling those encountered in  
1057 actual field measurements, was rather demanding on the  
1058 capabilities of most RT models. The entire birch stand  
1059 scene had to be illuminated but the transmission mea-  
1060 surements were restricted to small adjacent areas in the  
1061 center of the scene. This led to only two RT mod-  
1062 els contributing to this measurement type (`raytran` and  
1063 `Sprint3`). Figure 11 shows their local transmission sim-  
1064 ulations for transects oriented parallel (left panels) and  
1065 perpendicular (right panels) to the direction of the il-  
1066 lumination azimuth ( $\phi_i$ ) in both the red (top panels)  
1067 and NIR (bottom panels) spectral domain. Although the  
1068 simulation results are somewhat different, both models  
1069 capture obvious features in the spatial pattern of the lo-  
1070 cal canopy transmission. The various pink arrows indi-  
1071 cate obvious correlations with predominantly shadowed  
1072 and illuminated patches occurring along the transects de-  
1073 picted (in a perspective-free manner) at the top or bot-  
1074 tom of each of the four graphs. One should also note that  
1075 both models occasionally simulate local transmission val-  
1076 ues that are larger than unity (*i.e.*, they fall within the  
1077 grey shaded area at the top of each graph) which is an  
1078 unambiguous signature of the presence of horizontal radi-  
1079 ation fluxes. The occurrence of  $T > 1$  is somewhat more  
1080 frequent in the NIR due to the larger single-scattering  
1081 albedo ( $\omega_L = r_L + t_L$ ) of the foliage there, as well as for  
1082 transect orientations that are perpendicular to  $\phi_i$ , which  
1083 are the ones least affected by shadows from adjacent tree  
1084 crowns.

#### 4.2. The true zoom-in experiment

1085 The “true zoom-in” experiment was first proposed dur-  
1086 ing RAMI-2 (section 2.2 in *Pinty et al.* [2004b]) and con-  
1087 sists of a  $270 \times 270 \text{ m}^2$  scene featuring a number of spher-  
1088 ical and cylindrical volumes—having precisely defined  
1089 locations—that are filled with disc-shaped scatterers hav-

1090 ing different spectral properties (Table 5 and Figure 2 in  
1091 *Pinty et al.* [2004b]). The scene itself is illuminated over  
1092 its entire length whilst RT simulations are to be extracted  
1093 over a set of progressively smaller target areas located at  
1094 the center of the scene. The spatial resolutions of these  
1095 target areas are 270, 90 and 30 m, respectively. Such true  
1096 zoom-ins are useful when 1) the nature of local horizontal  
1097 fluxes—arising from the deterministic occurrence of  
1098 gaps and shadows in and immediately around the sam-  
1099 pling area—are to be studied/accounted for, and 2) the  
1100 creation of artificial “order”, due to cyclic boundary con-  
1101 ditions that reproduce the scene *ad infinitum*, has to be  
1102 avoided. The latter may arise when RT models have to  
1103 be executed on 3-D canopy representations at very high  
1104 spatial resolutions since the complexity of the scene is  
1105 such that spatially extensive representations cannot be  
1106 generated due to computer memory limitations.

1107 Within RAMI-3 the number of local patches in the  
1108 “true zoom-in” experiment was extended to nine, such  
1109 that the BRF simulations at 90 (30) m spatial resolu-  
1110 tion, when averaged over all nine patches equal that of  
1111 the (central) patch at the coarser 270 (90) m spatial  
1112 resolution since the TOC reference level remained the  
1113 same throughout the scene. The necessity for determin-  
1114 istic canopy representations and the complexity of the  
1115 RT simulation setup was, however, such that only **drat**,  
1116 **Sprint-3**, **raytran** and **Rayspread** performed all of these  
1117 simulations. Figure 12 thus restricts itself to total BRF  
1118 simulations in the principal (top panels) and orthogonal  
1119 (bottom panels) viewing planes for the 270 m (left), 90  
1120 m (middle) and 30 m (right) patches located at the cen-  
1121 ter of the scene (for which also simulations from **DART**  
1122 were available). The illumination zenith angle was set  
1123 to 20° and the spectral properties of the environment  
1124 feature typical NIR conditions. Going from coarse to  
1125 fine spatial resolutions (left to right panels in Figure 12)  
1126 one notices that the discrepancies between the various  
1127 model simulations increase both in the principal and or-  
1128 thogonal planes. In particular, it is the **DART** and the  
1129 **Sprint3** models that differ from the BRF simulations  
1130 of **drat**, **Rayspread** and **raytran**. Possible reasons for  
1131 these BRF differences include 1) a magnification of the  
1132 impact of small structural differences in the determin-  
1133 istic scene setup as the spatial resolution becomes finer,  
1134 and/or, 2) the occurrence of different patterns of shadow-  
1135 ing/illumination due to erroneously specified illumination  
1136 azimuth angles.

#### 1138 4.2.1. Local horizontal flux measurements

1139 In the visible part of the solar spectrum the divergence  
1140 of horizontal radiation in vegetation canopies is largely  
1141 controlled by the occurrence of mutual shadowing be-  
1142 tween individual canopy elements and photon channel-  
1143 ing through the gaps between them. As the canopy tar-  
1144 get becomes smaller the likelihood of non-zero horizontal  
1145 radiation balances increases, resulting in local radiative  
1146 regimes that are highly variable across the overall domain  
1147 of the canopy [*Widlowski et al.*, 2006b]. The interpreta-  
1148 tion, spatial distribution and up-scaling of *in situ* mea-  
1149 surements thus could benefit from a quantitative analysis  
1150 of the magnitude (and directionality) of horizontal radi-  
1151 ation transport, not only because this may contribute  
1152 toward the design of optimal sampling schemes for fu-  
1153 ture field validation campaigns, but also, because it may  
1154 allow the identification of site-specific spatial resolution  
1155 thresholds below which the pixel-based interpretation of  
1156 remotely sensed data may no longer be adequate (with-  
1157 out explicit accounting of horizontal radiation transport).

1158 RAMI-3 therefore introduced a horizontal flux measure-  
1159 ment for the “true zoom-in” canopy scene, where par-  
1160 ticipants were asked to simulate the total flux [W] that  
1161 entered and exited through the various sides of a vir-  
1162 tual voxel (box) encompassing the canopy at different  
1163 spatial resolutions. These voxels—which coincide both  
1164 in size and location with the local areas used for the  
1165 “true zoom-in” BRF simulations—extend to a height of  
1166 15 m and have their lateral sides either parallel (constant  
1167  $x$  coordinate) or perpendicular (constant  $y$  coordinate)  
1168 with the azimuth of the incident radiation,  $\phi_i$  (see Fig-  
1169 ure 13). As was the case for the local transmission tran-  
1170 sect measurement, only a couple of models (**Sprint-3**  
1171 and **raytran**) submitted results for the local horizontal  
1172 flux experiment. Figure 14 displays the results of these  
1173 simulations for voxel locations corresponding to the BRF  
1174 simulations depicted in Figure 12. More specifically, the  
1175 various entering (solid) and exiting (dashed) total hor-  
1176 izontal fluxes, normalised by the total incident flux at  
1177 the top of the canopy, are shown for voxels with spa-  
1178 tial dimensions equal to 270 m (left), 90 m (middle) and  
1179 30 m (right) in the NIR spectral domain. The illumina-  
1180 tion azimuth,  $\phi_i$  is parallel (perpendicular) to the voxel  
1181 sides labeled  $Y_{\text{LOW}}$  and  $Y_{\text{HIGH}}$  ( $X_{\text{LOW}}$  and  $X_{\text{HIGH}}$ ), and  
1182  $\theta_i = 20^\circ$ .

1183  
1184 The direct illumination component entering through  
1185 the sunward side of a voxel ( $X_{\text{HIGH}}$ ) and exiting through  
1186 its opposite side ( $X_{\text{LOW}}$ ) will naturally increase the mag-  
1187 nitude of the corresponding normalised fluxes with re-  
1188 spect to fluxes occurring in other directions and through  
1189 other lateral sides of the voxel. These latter fluxes, in  
1190 turn, can only arise from radiation that has been scat-  
1191 tered by the canopy/soil system, and tend to remain  
1192 directionally invariant in canopies with randomly dis-  
1193 tributed Lambertian scatterers [Widlowski *et al.*, 2006b].  
1194 By going from left to right in Figure 14, that is, from  
1195 relatively large voxels to smaller ones, it can be seen that  
1196 1) the differences between entering and exiting fluxes in-  
1197 crease, due to the increasingly non-random (and highly  
1198 deterministic) location of shadows and gaps, and 2) the  
1199 magnitude of the various horizontal fluxes increases, since  
1200 the ratio of the lateral and upper voxel sides increases  
1201 also. The total net horizontal flux of these voxels (*i.e.*,  
1202 the sum of all 4 laterally entering radiation streams mi-  
1203 nus the sum of the 4 laterally exiting radiation streams),  
1204 when normalised by the incident total flux at the TOC  
1205 level, was found to be of the order of  $-0.010$  ( $-10^{-4}$ )  
1206 at a spatial resolution of 270 m,  $-0.099$  ( $-0.002$ ) at 90  
1207 m, and  $0.038$  ( $0.007$ ) at 30 m by the model **Sprint3**  
1208 (**raytran**). One should note that **Sprint3** deviates by  $\sim 1$   
1209 % from the zero net horizontal radiation transport that  
1210 energy conservation dictates at a spatial resolution of 270  
1211 m – since here the entire scene is contained within the  
1212 voxel. The increasing magnitude of the net lateral radi-  
1213 ation exchanges as function of spatial resolution is, how-  
1214 ever, confirmed by both models. This behaviour has to  
1215 be accounted for when deriving domain-averaged canopy  
1216 transmission, absorption or reflectance estimates on the  
1217 basis of a series of local point measurements, *e.g.*, Tian  
1218 *et al.* [2002]; Gobron *et al.* [2006].

### 4.3. The conifer forest

1219 The “conifer forest” scene was originally proposed  
1220 during RAMI-2 with the aim of simulating the radia-  
1221 tive transfer regime in structurally heterogeneous scenes  
1222 of rather large spatial extent ( $500 \times 500 \text{ m}^2$ ) that fea-  
1223 tured tree architectures and spectral properties reflecting  
1224 those of typical coniferous forests (overlying a snow back-

ground). The RAMI-2 specifications of the “conifer forest” included conical tree crown representations (of fixed dimensions) that were distributed uniformly over a Gaussian shaped hill surface. In RAMI-3 a non-topography version of the same coniferous forest was added in order to investigate whether the deviations in the RT simulations in the Gaussian hill scenario were solely due to the topography itself. Both implementations of the “conifer forest” feature identical numbers and sizes of trees. Figure 15 displays the model simulated BRFs in the principal (top 2 rows) and orthogonal (bottom 2 rows) viewing planes for the “conifer forest” scene with topography (left panels), without topography (middle panels), and the difference between these two (right panels). Simulations pertain to the red (top and third row) and near-infrared (second and bottom row) spectral regimes of the canopy, and  $\theta_i = 40^\circ$ .

One notices the close agreement between the BRF simulations of the models `drat`, `Rayspread`, `raytran`, and `Sprint3` in all of the test cases. The `MAC` model provided identical simulations for both the flat background and the Gaussian hill scenarios. Both of these tend to be higher than the BRF values from most other models, however. The `5Scale` model, which utilises a cylinder and a cone to represent the shape of the tree crowns, generates somewhat higher BRF values in the red spectral domain and somewhat lower BRF values in the NIR spectral domain. Accounting for the reduced number of models participating in the Gaussian hill case, one may say that, overall, the envelope of all the BRF simulations in the Gaussian hill scenario is very similar to that in the flat background case. The impact of topography becomes, however, noticeable when subtracting the BRF simulations in the flat background case from those of the corresponding Gaussian hill scenario (right column) – in particular at large view zenith angles. For observations close to nadir, on the other hand, few topography-induced differences can be observed since both “conifer forest” representations feature identical canopy statistics (*e.g.*, LAI, tree number, fractional cover, *etc.*). In the principal plane the presence of a hill shaped background thus leads to enhanced BRFs in the backward scattering direction (*i.e.*, a large amount of radiation is reflected back from the illuminated slopes of the hill), and reduced BRFs in the forward scattering direction (*i.e.*, little reflection from that part of the scene that lies in the shadow of the hill). In the orthogonal plane, the Gaussian hill BRFs exceed those of the flat background case at large view zenith angles because of the larger contribution from the snowy slopes of the Gaussian hill (*i.e.*, the single-uncollided BRF component). In the NIR, this effect is somewhat dampened by the single-collided and multiple-collided BRF components, which tend to be larger in the flat background case. The absolute impact that the Gaussian hill exerts on the simulated BRFs thus tends to be more noticeable in the red than the NIR spectral regime.

#### 4.4. The “floating spheres” purist corner

Adding conservative scattering conditions in heterogeneous canopy environments allows to push the RT formulations of 3-D models to their limits, in particular with respect to the multiple scattered radiation component. RAMI-3 thus proposed to run the “floating spheres” test cases under purist corner conditions, *i.e.*, with  $r_l = t_l = 0.5$  and  $\alpha = 1$ . Seven RT models participated in these test cases and their simulation results are shown in Figure 16. More specifically, the total BRFs in the principal (left columns) and orthogonal (right columns) planes for discrete (top row) and turbid medium (bottom row)

1292 “floating spheres” representations at two different illu-  
1293 mination zenith angles ( $\theta_i = 20^\circ$  and  $50^\circ$ ) under purist  
1294 corner conditions are shown. The structure of the scenes  
1295 is indicated in the inlaid images. One can see that, simi-  
1296 lar to the solar domain simulations, the 3-D Monte Carlo  
1297 models `drat`, `Rayspread`, `raytran`, and `Sprint3` gener-  
1298 ated very similar results, with both DART and FRT being  
1299 somewhat different in the turbid and discrete cases. The  
1300 `4SAIL2` model, on the other hand, generates significantly  
1301 higher BRFs than the other models.

#### 4.5. Overall model performances in RAMI-3

1302 There is an expectation that the RAMI activity should  
1303 provide an overall indication of the performance of a  
1304 given model. This is, however, not a trivial task,  
1305 since there is a need to account for the reliability of  
1306 the model simulations, the number of experiments per-  
1307 formed, and the computer processing time that was re-  
1308 quired to do these simulations. Instead, Figure 17 pro-  
1309 vides an overview of the participation and model-to-  
1310 ensemble performance of the various models that con-  
1311 tributed toward RAMI-3. Statistics are provided for to-  
1312 tal BRF simulations over structurally homogeneous (top  
1313 table) and heterogeneous (bottom table) discrete canopy  
1314 representations. The various model names are listed on  
1315 the top of each table (one per column). The experiment  
1316 identifier is provided to the left, whereas the spectral  
1317 regime is indicated to the right of each table column.  
1318 Light (dark) grey fields indicate incomplete (no) data  
1319 submission. The green-yellow-red colour scheme rep-  
1320 resents the overall model-to-ensemble difference,  $\bar{\delta}_m$  quan-  
1321 tifying the dispersion that exists between a given model  
1322  $m$  and all other models that have performed the complete  
1323 set of prescribed total BRF simulations for the experi-  
1324 ment/spectral regime combination of interest. One will  
1325 note that almost all models—whether analytic, stochas-  
1326 tic, hybrid, or Monte Carlo—agree to within 2–4 % with  
1327 the ensemble of all other models in the homogeneous  
1328 cases. The MBRF model stands out as being somewhat  
1329 different from the other RAMI-3 participants. In the  
1330 heterogeneous case, the 3-D MC models tend to be in  
1331 good agreement with the ensemble of model simulations,  
1332 whereas models with structural and radiative approxima-  
1333 tions/parameterisation deviate somewhat more - as was  
1334 discussed and documented in the various previous sub-  
1335 sections. One should note that the predominant hue in  
1336 the  $\bar{\delta}_m$  colours of any given row in Figure 17 depends  
1337 both on the degree and manner in which the models are  
1338 dispersed around the main cluster of simulation results.  
1339 The mostly red colours characterising  $\bar{\delta}_m$  for the discrete  
1340 “floating spheres” canopies in the NIR spectral domain  
1341 (second last row in lower panel), for example, are due  
1342 to the consistently large deviations of the `5Scale` and  
1343 `4SAIL2` simulations with respect to each other and to the  
1344 cluster of 3D Monte Carlo models. Finally, the large,  
1345 noticeable, amount of (light and dark) grey patches in  
1346 Figure 17 indicate that a significant number of experi-  
1347 ments were not completed or submitted.

## 5. Concluding remarks

1348 The third phase of the Radiation transfer Model In-  
1349 tercomparison (RAMI) activity with its record participa-  
1350 tion, its extensive set of new experiments and measure-  
1351 ments, and its substantially improved agreement between  
1352 3-D MC models sets a milestone in the evolution of the  
1353 RT modelling community. It is now estimated that about  
1354 60 - 65% of all currently existing canopy reflectance mod-

1355 els have voluntarily participated at some time or other in  
1356 the RAMI initiative. Through its continuing support and  
1357 active encouragement of RAMI the RT modelling com-  
1358 munity has demonstrated maturity 1) by acknowledging  
1359 the necessity for quality assured RT models if these are  
1360 to be applied to the interpretation of remotely sensed  
1361 data, 2) by voluntarily contributing to the establishment  
1362 of benchmarking scenarios against which future develop-  
1363 ments of RT models may be evaluated, and 3) by agree-  
1364 ing to publish their model simulations in the refereed  
1365 scientific literature prior to knowing the results of the  
1366 intercomparison exercise. Since its first phase in 1999,  
1367 RAMI has served as a vehicle to document the perfor-  
1368 mance of the latest generation of RT models by charting  
1369 both their capabilities and weaknesses under a variety  
1370 of spectral and structural conditions. During RAMI-3 it  
1371 has been possible to actually demonstrate, for the first  
1372 time, a general convergence of the ensemble of submitted  
1373 RT simulations (with respect to RAMI-2), and to doc-  
1374 ument the unprecedented level of agreement that now  
1375 exists between the participating 3-D Monte Carlo mod-  
1376 els. These positive developments do not only further the  
1377 confidence that may be placed in the quality of canopy  
1378 reflectance models, but they also pave the way for ad-  
1379 dressing new and challenging issues, most notably, in the  
1380 context of supporting field validation efforts of remotely  
1381 sensed products. The latter is of prime importance given  
1382 the abundance of global surface products from the cur-  
1383 rent fleet of instruments, like MISR, MODIS, MERIS,  
1384 *etc.* The usage of quality-assured RT models in detailed  
1385 simulations of *in situ* field measurements at very high  
1386 spatial resolutions is thus only a first step toward propos-  
1387 ing optimal sampling/up-scaling schemes that guarantee  
1388 accurate domain-averaged absorption, transmission, *etc.*  
1389 estimates. RAMI-3 has, however, also shown that only a  
1390 few models are currently able to perform such kinds of RT  
1391 simulations. The challenge thus lies with the modelling  
1392 community as a whole to provide the scientists involved  
1393 in field validation campaigns of satellite derived surface  
1394 products with optimal sampling practices that are rooted  
1395 in a proper understanding of the radiative transfer in ar-  
1396 chitecturally complex 3-D media.

1397

### 5.1. Structurally divergent model premises

1398 More models than ever participated in the third phase  
1399 of RAMI, and the agreement between them, in particu-  
1400 lar for the various baseline scenarios, has noticeably in-  
1401 creased with respect to previous phases of RAMI (Fig-  
1402 ure 7). The continuation of the strategy adopted during  
1403 RAMI-2, *i.e.*, to provide detailed descriptions of the posi-  
1404 tion and orientation of every single leaf in scenes with dis-  
1405 crete foliage representations, as well as indications of all  
1406 tree/crown locations in the relevant scenes on the RAMI  
1407 website, has—among other factors—contributed to im-  
1408 proving the agreement among the various 3-D MC RT  
1409 models (Figures 6, 8, 10, 16 and Table 2). This devel-  
1410 opment provides further weight to using these models in  
1411 defining a “surrogate truth” that may then be used—even  
1412 for structurally heterogeneous canopy architectures—to  
1413 obtain an indication of the performance of other RT mod-  
1414 els. It may be argued, however, that such an approach  
1415 is only meaningful if all the models implement identical  
1416 canopy representations in their RT simulations. Both  
1417 the deviations in the structural premises of a RT model  
1418 and the approximations and/or errors in the implementa-  
1419 tion of the model’s radiative transfer formulation may be  
1420 held responsible for the observed BRF/flux differences.  
1421 If the purpose of RAMI were solely to identify RT re-

1422 lated differences in canopy reflectance models, then the  
1423 current flexibility in the implementation of RAMI test  
1424 cases would have to be replaced by rigorously specified  
1425 canopy architectures that were specifically tailored to the  
1426 scene description formalism of each and every partici-  
1427 pating RT model. Alternatively, the derivation and use  
1428 of “effective” state variables may be proposed to poten-  
1429 tial RAMI participants, since recent findings, *e.g.*, *Cairns*  
1430 *et al.* [2000]; *Pinty et al.* [2006]; *Widlowski et al.* [2005],  
1431 have suggested that diverging target structures may still  
1432 yield identical radiative properties provided that “effec-  
1433 tive” instead of actual state variable values are avail-  
1434 able for RT simulations (one possible approach to derive  
1435 such effective state variables is described in *Pinty et al.*  
1436 [2004a]).

1437  
1438 Ultimately, however, it is the accuracy of the retrieved  
1439 state variable values that counts in RT model applica-  
1440 tions. The logical consequence of this line of reasoning  
1441 thus would be to address the inversion of RT models  
1442 in the context of RAMI against predefined sets of spec-  
1443 tral and angular observations, similar to those provided  
1444 by the current fleet of space borne sensors, *e.g.*, ATSR-  
1445 2/AATSR [*Stricker et al.*, 1995], CHRIS-Proba [*Barnsley*  
1446 *et al.*, 2004], MISR [*Diner et al.*, 2002], and POLDER  
1447 [*Deschamps et al.*, 1994]. In this way, the impact that  
1448 the various structural and radiative formalisms in the  
1449 RT models may have with respect to the values of the re-  
1450 trieved state variables could then be assessed in the light  
1451 of the known uncertainties in the available surface BRFs.  
1452 Indeed, during RAMI-1 a set of “inverse mode” scenar-  
1453 ios had been proposed but this had been abandoned in  
1454 subsequent phases due to a lack of participants. Given  
1455 the close agreement of the various participating models in  
1456 RAMI-3, it may become appropriate to revisit this issue  
1457 in the future.

## 5.2. The RAMI On-line model checker (ROMC)

1458 One of the positive outcome of RAMI-3 is the consis-  
1459 tently good agreement (see Table 2) between simulation  
1460 results of a small set of 3-D MC models – and this both  
1461 over homogeneous as well as heterogeneous vegetation  
1462 canopies. It thus is feasible to derive a “surrogate truth”  
1463 for almost all of the measurements and experiments fea-  
1464 tured within RAMI (current exceptions are the “local  
1465 transmission transects”, the “local horizontal fluxes” and  
1466 some of the BRF simulations relating to the 30 m spa-  
1467 tial resolution patches in the “true zoom-in” experiment).  
1468 With this valuable dataset at hand, it becomes possible  
1469 to allow model owners, developers and customers to evalu-  
1470 ate the performance of a given RT model even outside  
1471 the frame of a RAMI phase. To facilitate such an under-  
1472 taking the RAMI On-line Model Checker (ROMC) was  
1473 developed at the Joint Research Centre of the European  
1474 Commission in Ispra, Italy. The ROMC is a web-based  
1475 interface allowing for the on-line evaluation of RT mod-  
1476 els using as reference the “surrogate truth” derived from  
1477 among the 6 Monte Carlo models **DART**, **drat**, **FLIGHT**,  
1478 **Rayspread**, **raytran** and **Sprint3** using an appropriate  
1479 set of selection criteria (see section 3.3.3). Access to  
1480 the ROMC can be obtained either via the RAMI web-  
1481 site or directly using the URL <http://romc.jrc.it/><sup>4</sup>.  
1482 After providing a username and valid email address, the  
1483 ROMC can be utilised in two different ways: 1) in **debug**  
1484 **mode**, which allows to *repeatedly* compare the output of  
1485 a RT model to that of one or more experiments and/or  
1486 measurements from RAMI, *i.e.*, the simulation results  
1487 are available on the RAMI website, and 2) in **validate**  
1488 **mode**, which enables the *once-only* testing of the RT

1489 model against a continuously changing set of test cases  
1490 that are similar but not quite equivalent to those from  
1491 RAMI, *i.e.*, the solutions are not known *a priori* and the  
1492 experiments cannot be repeated.

1493

1494 • In **debug mode** users may choose to execute one  
1495 particular experiment and/or measurement from the set  
1496 of RAMI-3 test cases *ad infinitum*, or, at least until they  
1497 are satisfied with the performance of their model. De-  
1498 tailed descriptions of the structural, spectral, illumina-  
1499 tion and measurement conditions are available. Once the  
1500 model simulation results are generated, they can be up-  
1501 loaded via the web-interface, and—provided they adhere  
1502 to the RAMI filenames and formatting conventions—  
1503 this process will result in a series of graphical results files  
1504 being made available for all test cases. In debug mode  
1505 users may not only download their ROMC results but  
1506 also an ASCII file containing the actual “surrogate truth”  
1507 data.

1508 • In **validate mode** users may choose between  
1509 structurally homogeneous and/or heterogeneous “float-  
1510 ing spheres” canopies to verify the performance of their  
1511 model. The actual set of test cases will, however, be  
1512 drawn randomly from a large list of possible ones, such  
1513 that it is unlikely to obtain the same test case twice,  
1514 *i.e.*, in all likelihood one will not “know” the solution  
1515 *a priori*. Again, the “surrogate truth” was derived from  
1516 simulations generated by models belonging to the same  
1517 set of 3-D MC models as was the case for the debug  
1518 mode. In validate mode the reference data will, however,  
1519 not be available for downloading. The procedure for data  
1520 submission, on the other hand, is identical to that of the  
1521 debug mode, and—provided that all RAMI formatting  
1522 and filenames requirements were applied—will also lead  
1523 to a results page featuring a variety of intercomparison  
1524 graphics.

1525

1526 Users may download their ROMC results either as jpeg  
1527 formatted images from the ROMC website, or else, opt  
1528 for receiving them via email in postscript form. Both  
1529 the debug and validate mode ROMC results files feature  
1530 a reference number and a watermark. Available graphs  
1531 include: Plots of both the model and reference BRFs  
1532 in the principal or orthogonal plane, 1 to 1 plots of the  
1533 model and reference BRFs, histograms of the deviations  
1534 between model and reference BRFs,  $\chi^2$  graphs for all sub-  
1535 mitted measurements using an  $f$  value of 3% as well as,  
1536 graphs depicting the deviation of the model and reference  
1537 fluxes using barcharts. Users of ROMC are encouraged  
1538 to utilise only ROMC results that were obtained in val-  
1539 idate mode for publications. Those obtained in debug  
1540 mode, obviously, do not qualify as proof regarding the  
1541 performance of a RT model since all simulation results  
1542 may readily be viewed on the RAMI website. Last but  
1543 not least, a large ensemble of FAQs should help to guide  
1544 the user through the ROMC applications. It is hoped  
1545 that the ROMC will prove useful for the RT modelling  
1546 community, not only by providing a convenient means to  
1547 evaluate RT models outside the triennial phases of RAMI  
1548 (something that was rather tedious in the past if authors  
1549 wished to rely on the experiences gained from RAMI,  
1550 *e.g.*, *Gastellu-Etcheberry et al.* [2004]) but also to attract  
1551 participation in future RAMI activities.

1552

### 5.3. Future perspectives for RAMI

1553 RAMI was conceived as an open-access community ex-  
1554 ercise and will continue to pursue that direction. As such

1555 it's goal is to move forward in a manner that addresses  
1556 the needs of the majority of RT model (developers and  
1557 users). For example, relatively simple RT modelling ap-  
1558 proaches designed only to simulate integrated fluxes, like  
1559 the **2-Stream** model, should not be neglected in future  
1560 developments of RAMI due the large communities in-  
1561 volved with soil-vegetation-atmosphere transfer (SVAT)  
1562 models, as well as general circulation models. Whereas  
1563 such two stream approaches remove all dependencies on  
1564 vegetation structure beyond leaf quantity and orienta-  
1565 tion, the various findings of RAMI-3, and in particular  
1566 the above discussion, have highlighted the relevance of  
1567 canopy structure in forward mode RT simulations. With  
1568 every model having its own implementation of "reality" it  
1569 may be appropriate to provide as detailed descriptions as  
1570 possible of highly realistic canopy architectures in future  
1571 phases of RAMI (see for example *Disney et al.* [2006]).  
1572 Various techniques are currently available for the genera-  
1573 tion of realistic 3-D trees, the most well known one being  
1574 probably the L-systems approach, *e.g.*, *Prusinkiewicz and*  
1575 *Lindenmayer* [1990]; *Weber and Penn* [1995]; *De Reffye*  
1576 *and Houllier* [1997]. Using these methodologies to gener-  
1577 ate a detailed depiction of the architectural character-  
1578 istics of (part of) well documented sites—like BOREAS  
1579 [*Sellers et al.*, 1997] and/or the Kalahari transect (SA-  
1580 FARI 2000) [*Scholes et al.*, 2004], for example—would  
1581 allow to 1) study the variability in the radiative surface  
1582 properties predicted by a whole suite of participating RT  
1583 models, as well as their possible impact on the hydro-  
1584 logical and carbon cycles, 2) investigate by how much  
1585 RT model simulations vary when carried out on the basis  
1586 of canopy representations with a progressively increasing  
1587 degree of structural abstractions (all state variable val-  
1588 ues remain constant, or are converted to "effective" val-  
1589 ues), *e.g.*, *Smolander and Stenberg* [2005]; *Rochdi et al.*  
1590 [2006], 3) compare such surface BRF simulations with  
1591 atmospherically-corrected observations from space borne  
1592 instruments, 4) investigate the potential of RT models  
1593 to reproduce *in situ* measurements of transmitted light,  
1594 *e.g.*, Tracing Radiation and Architecture of Canopies  
1595 (TRAC) instrument [*Chen and Cihlar*, 1995; *Leblanc*,  
1596 2002], and/or hemispherical photographs [*Leblanc et al.*,  
1597 2005; *Jonckheere et al.*, 2005], and 5) assess the accuracy  
1598 of up-scaling methodologies currently used in validation  
1599 efforts of satellite derived products like FAPAR and LAI,  
1600 *e.g.*, *Morisette et al.* [2006]. In this way RAMI can ac-  
1601 tively contribute towards systematic validation efforts of  
1602 RT models, operational algorithms, and field instruments  
1603 – as promoted by the Committee on Earth Observation  
1604 Satellites (CEOS).

1605 **Acknowledgments.** The definition of the RAMI test  
1606 cases on a dedicated website, the coordination of the RAMI  
1607 participants, and the analysis of the submitted simulation re-  
1608 sults would not have been possible without the financial sup-  
1609 port of the European Commission, and more specifically, the  
1610 Global Environment Monitoring unit of the Institute for Envi-  
1611 ronment and Sustainability in the DG Joint Research Centre.  
1612 The valuable comments of the three anonymous reviewers and  
1613 the stimulating exchanges with the various scientists of the  
1614 RAMI Advisory Body (RAB), as well as those involved with  
1615 the I3RC, are also gratefully acknowledged.

## Notes

1. Due to the renaming of all European Commission web-  
sites this URL is likely to change in the near future to  
<http://rami-benchmark.jrc.ec.europa.eu/>

2. Canopy structure is defined here as the (statistical or deterministic) description of locations and orientations of foliage and woody constituents within the three-dimensional space of a RAMI scene.
3. Due to the renaming of all European Commission websites this URL is likely to change in the near future to <http://romc.jrc.ec.europa.eu/> .
4. See footnote 3.

## References

---

## References

- 1621 Barnsley, M. J., J. J. Settle, M. Cutter, D. Lobb, and  
1622 F. Teston, The PROBA/CHRIS mission: a low-cost small-  
1623 sat for hyperspectral, multi-angle, observations of the Earth  
1624 surface and atmosphere, *IEEE Transactions on Geoscience  
1625 and Remote Sensing*, 42, 1512–1520, 2004.
- 1626 Bruegge, C. J., N. L. Chrien, R. R. Ando, D. J. Diner, W. A.  
1627 Abdou, M. C. Helmlinger, S. H. Pilorz, and K. J. Thome,  
1628 Early validation of the Multi-angle Imaging SpectroRa-  
1629 diometer (ISR) radiometric scale, *IEEE Transactions on  
1630 Geoscience and Remote Sensing*, 40, 1477–1492, 2002.
- 1631 Bunnik, N. J. J., The multispectral reflectance of shortwave  
1632 radiation of agricultural crops in relation with their mor-  
1633 phological and optical properties, *Tech. rep.*, Mededelin-  
1634 gen Landbouwhogeschool, Wageningen, The Netherlands,  
1635 1978.
- 1636 Cahalan, R. F., L. Oreopoulos, A. Marshak, K. F. Evans, A. B.  
1637 Davis, R. Pincus, K. Yetzer, B. Mayer, R. Davies, T. Ack-  
1638 erman, H. Barker, E. Clothiaux, R. Ellingson, M. Garay,  
1639 E. Kassianov, S. Kinne, A. Macke, W. OHirok, P. Partain,  
1640 S. Prigarin, A. Rublev, G. Stephens, F. Szczap, E. Takara,  
1641 T. Vrnai, G. Wen, and T. Zhuravleva, The international  
1642 intercomparison of 3D radiation codes (I3RC): Bringing to-  
1643 gether the most advanced radiative transfer tools for cloudy  
1644 atmospheres, *Bulletin of the American Meteorological So-  
1645 ciety*, 86, 1275–1293, 2005.
- 1646 Cairns, B., A. Lacis, and B. Carlson, Absorption within inho-  
1647 mogeneous clouds and its parameterization in general cir-  
1648 culation models, *Journal of the Atmospheric Sciences*, 57,  
1649 700–714, 2000.
- 1650 Campbell, G. S., Derivation of an angle density function for  
1651 canopies with ellipsoidal leaf angle distribution, *Agricul-  
1652 tural and Forest Meteorology*, 49, 173–176, 1990.
- 1653 Chen, J. M., and J. Cihlar, Plant canopy gap size analysis the-  
1654 ory for improving optical measurements of leaf area index,  
1655 *Applied Optics*, 34, 6211–6222, 1995.
- 1656 Chen, J. M., J. Liu, S. G. Leblanc, R. Lacaze, and J. L.  
1657 Roujean, Multi-angular optical remote sensing for assess-  
1658 ing vegetation structure and carbon absorption, *Remote  
1659 Sensing Environment*, 84, 516–525, 2003.
- 1660 Chopping, M. J., A. Rango, K. M. Havstad, F. R. Schiebe,  
1661 J. C. Ritchie, T. J. Schmutge, A. N. French, L. Su, L. Mc-  
1662 Kee, and R. Davis, Canopy attributes of desert grasslands  
1663 and transition communities derived from multi-angular air-  
1664 borne imagery, *Remote Sensing Environment*, 85, 339–354,  
1665 2003.
- 1666 De Reffye, P., and F. Houllier, Modelling plant growth and  
1667 architecture: Some recent advances and applications to  
1668 agronomy and forestry, *Current Science*, 73, 984–992, 1997.
- 1669 Deschamps, P. Y., F.-M. Bréon, M. Leroy, A. Podaire,  
1670 A. Bricaud, J.-C. Buriez, and G. Sèze, The POLDER mis-  
1671 sion: Instruments characteristics and scientific objectives,  
1672 *IEEE Transactions on Geosciences and Remote Sensing*,  
1673 32, 586–615, 1994.
- 1674 Diner, D. J., J. C. Beckert, G. W. Bothwell, and J. I. Ro-  
1675 drigues, Performance of the MISR instrument during its  
1676 first 20 months in Earth orbit, *IEEE Transactions on Geo-  
1677 science and Remote Sensing*, 40, 1449–1466, 2002.
- 1678 Dirmeyer, P. A., A. J. Dolman, and N. Sato, The global soil  
1679 wetness project: A pilot project for global land surface  
1680 modeling and validation, *Bulletin of the American Meeo-  
1681 rological Society*, 80, 851–878, 1999.
- 1682 Disney, M. I., P. Lewis, and P. R. J. North, Monte Carlo  
1683 raytracing in optical canopy reflectance modelling, *Remote  
1684 Sensing Reviews*, 18, 163–196, 2000.
- 1685 Disney, M. I., P. Lewis, and P. Saich, 3D modelling of for-  
1686 est canopy structure for remote sensing simulations in the  
1687 optical and microwave domains, *Remote Sensing of Envi-  
1688 ronment*, 100, 114–132, 2006.

1689 Fernandes, R. A., L. S. G., and S. A., A multi-scale analytical  
1690 canopy (MAC) reflectance model based on the angular  
1691 second order gap size distribution, in *Proceedings of the*  
1692 *international geoscience and remote sensing symposium*,  
1693 vol. 7, pp. 4431–4433, 2003.

1694 Gastellu-Etchegorry, J.-P., V. Demarez, V. Pinel, and  
1695 F. Zagolski, Modeling radiative transfer in heterogeneous  
1696 3-d vegetation canopies, *Remote Sensing of Environment*,  
1697 58, 131–156, 1996.

1698 Gastellu-Etchegorry, J.-P., E. Martin, and F. Gascon, Dart:  
1699 a 3D model for simulating satellite images and studying  
1700 surface radiation budget, *International Journal of Remote*  
1701 *Sensing*, 25, 73–96, 2004.

1702 Gates, W. L., J. Boyle, C. Covey, C. Dease, C. Doutriaux,  
1703 R. Drach, M. Fiorino, P. Gleckler, J. Hnilo, S. Marlais,  
1704 T. Phillips, G. Potter, B. Santer, K. Sperber, K. Taylor,  
1705 and D. Williams, An overview of the results of the atmo-  
1706 spheric model intercomparison project (AMIP I), *Bulletin*  
1707 *of the American Meteorological Society*, 73, 1962–1970,  
1708 1998.

1709 Gerard, F. F., and P. R. J. North, Analyzing the effect of struc-  
1710 tural variability and canopy gaps on forest BRDF using a  
1711 geometric-optical model, *Remote Sensing of Environment*,  
1712 62, 46–62, 1997.

1713 Gerstl, S. A. W., Angular reflectance signature of the canopy  
1714 hotspot in the optical regime, in *4th Intl. Coll. On Spectral*  
1715 *Signatures of Objects in Remote Sensing, Aussois, France*,  
1716 p. 129, ESA report SP-287, 1988.

1717 Gobron, N., B. Pinty, M. M. Verstraete, and Y. Govaerts, A  
1718 semi-discrete model for the scattering of light by vegetation,  
1719 *Journal of Geophysical Research*, 102, 9431–9446, 1997.

1720 Gobron, N., B. Pinty, O. Aussedat, J. M. Chen, W. B. Co-  
1721 hen, R. Fensholt, V. Gond, K. F. Huemmrich, T. Lavergne,  
1722 F. Mélin, J. L. Privette, I. Sandholt, M. Taberner, D. P.  
1723 Turner, M. M. Verstraete, and J.-L. Widlowski, Evaluation  
1724 of FAPAR products for different canopy radiation trans-  
1725 fer regimes: Methodology and results using JRC prod-  
1726 ucts derived from SeaWiFS against ground-based estima-  
1727 tions, *Journal of Geophysical Research*, 111, D13100, doi:  
1728 10.1029/2005/JD006511, 2006.

1729 Goel, N. S., and D. E. Strelbel, Simple beta distribution repre-  
1730 sentation of leaf orientation in vegetation canopies, *Agron-*  
1731 *omy Journal*, 76, 800–803, 1984.

1732 Govaerts, Y., and M. M. Verstraete, Raytran: A Monte Carlo  
1733 ray tracing model to compute light scattering in three-  
1734 dimensional heterogeneous media, *IEEE Transactions on*  
1735 *Geoscience and Remote Sensing*, 36, 493–505, 1998.

1736 Helbert, J., B. Berthelot, and C. Soler, Hyemalis: Un  
1737 simulateur d’images de paysages tridimensionnels com-  
1738 plexes, in *Revue Française de Photogrammétrie et de*  
1739 *Téledétection*, 173 / 174, pp. 27–35, Société Française de  
1740 Photogrammétrie et de Télédection, 2003.

1741 Henderson-Sellers, A., A. J. Pitman, P. K. Love, P. Iranne-  
1742 jad, and T. Chen, The project for intercomparison of land  
1743 surface parameterisation schemes (PILPS): Phases 2 and 3.,  
1744 *Bulletin of the American Meteorological Society*, 76, 489–  
1745 503, 1995.

1746 Jonckheere, I., B. Muys, and P. Coppin, Assessment of auto-  
1747 matic gap fraction estimation of forests from digital hemi-  
1748 spheric photography, *Agricultural and Forest Meteorol-*  
1749 *ogy*, 132, 96–114, 2005.

1750 Kneubühler, M., M. Schaepman, K. Thome, F. Baret, and  
1751 A. Müller, Calibration and validation of Envisat MERIS.  
1752 Part 1: vicarious calibration at Rail Road valley Playa  
1753 (NV), in *Proceedings of MERIS level 2 validation Work-*  
1754 *shop, ESRIN, Frascati, Italy, December 9–13, 2002*.

1755 Kuusk, A., The hot spot effect in plant canopy reflectance, in  
1756 *Photon-Vegetation Interactions*, edited by R. Myneni and  
1757 J. Ross, pp. 139–159, Springer-Verlag, New York, 1991.

1758 Kuusk, A., A two-layer canopy reflectance model, *Journal of*  
1759 *Quantitative Spectroscopy and Radiative Transfer*, 71, 1–9,  
1760 2001.

1761 Kuusk, A., and T. Nilson, A directional multispectral forest re-  
1762 flectance model, *Remote Sensing of Environment*, 72, 244–  
1763 252, 2000.

1764 Latif, M., K. Sperber, J. Arblaster, P. Braconnot, D. Chen,  
1765 A. Colman, U. Cubasch, M. Davey, P. Delecluse, D. De-

1766 Witt, L. Fairhead, G. Flato, T. Hogan, M. Ji, M. Kimoto,  
1767 A. Kitoh, T. Knutson, H. Le Treut, T. Li, S. Manabe,  
1768 O. Marti, C. Mechoso, G. Meehl, S. Power, E. Roeckner,  
1769 J. Sirven, L. Terray, A. Vintzileos, R. Voß, B. Wang,  
1770 W. Washington, I. Yoshikawa, J. Yu, and S. Zebiak, ENSIP:  
1771 The El Niño simulation intercomparison project, *Climate*  
1772 *Dynamics*, 18, 255–276, 2001.

1773 Leblanc, S. G., Correction to the plant canopy gap size analy-  
1774 sis theory used by the Tracing Radiation and Architecture  
1775 of Canopies (TRAC) instrument, *Applied Optics*, 31, 7667–  
1776 7670, 2002.

1777 Leblanc, S. G., and J. M. Chen, A windows graphic user in-  
1778 terface (GUI) for the five-scale model for fast BRDF simu-  
1779 lations, *Remote Sensing Reviews*, 19, 293–305, 2001.

1780 Leblanc, S. G., J. M. Chen, R. Fernandes, D. W. Deering, and  
1781 A. Conley, Methodology comparison for canopy structure  
1782 parameters extraction from digital hemispherical photogra-  
1783 phy in boreal forests, *Agricultural and Forest Meteorology*,  
1784 129, 187–207, 2005.

1785 Lewis, P., Three-dimensional plant modelling for remote sens-  
1786 ing simulation studies using the botanical plant modelling  
1787 system, *Agronomie - Agriculture and Environment*, 19,  
1788 185–210, 1999.

1789 Lovell, J. L., and R. D. Graetz, Analysis of POLDER-ADEOS  
1790 data for the Australian continent: the relationship between  
1791 BRDF and vegetation structure, *International Journal of*  
1792 *Remote Sensing*, 23, 2767–2796, 2002.

1793 Morisette, J. T., F. Baret, J. L. Privette, R. B. Myneni,  
1794 J. Nickeson, S. Garrigue, N. Shabanov, M. Weiss, R. Fer-  
1795 nandes, S. Leblanc, M. Kalacska, G. A. Sánchez-Azofeifa,  
1796 M. Chubey, B. Rivard, P. Stenberg, M. Rautiainen,  
1797 P. Voipio, T. Manninen, A. Pilant, T. Lewis, J. James,  
1798 R. Colombo, M. Meroni, L. Busetto, W. Cohen, D. Turner,  
1799 E. D. Warner, G. W. Petersen, G. Seufert, and R. Cook,  
1800 Validation of global moderate resolution LAI products: a  
1801 framework proposed within the CEOS Land Product Val-  
1802 idation subgroup, *IEEE Transactions on Geoscience and*  
1803 *Remote Sensing*, 44, 1804–1817, 2006.

1804 North, P. R. J., Three-dimensional forest light interaction  
1805 model using a Monte Carlo method, *IEEE Transactions*  
1806 *on Geoscience and Remote Sensing*, 34, 946–956, 1996.

1807 Oreskes, N., K. Shrader-Frechette, and K. Belitz, Verification,  
1808 validation, and confirmation of numerical models in the  
1809 earth sciences, *Science*, 263, 641–646, 1994.

1810 Pinty, B., N. Gobron, J.-L. Widlowski, S. A. W. Gerstl,  
1811 M. M. Verstraete, M. Antunes, C. Bacour, F. Gascon, J.-  
1812 P. Gastellu, N. Goel, S. Jacquemoud, P. North, W. Qin,  
1813 and R. Thompson, The RAdiation transfer Model Inter-  
1814 comparison (RAMI) exercise, *Journal of Geophysical Re-*  
1815 *search*, 106, 11,937–11,956, 2001.

1816 Pinty, B., N. Gobron, J.-L. Widlowski, T. Lavergne, and M. M.  
1817 Verstraete, Synergy between 1-D and 3-D radiation trans-  
1818 fer models to retrieve vegetation canopy properties from re-  
1819 mote sensing data, *Journal of Geophysical Research*, 109,  
1820 D21205, doi:10.1029/2004JD005214, 2004a.

1821 Pinty, B., J.-L. Widlowski, M. Taberner, N. Gobron, M. M.  
1822 Verstraete, M. Disney, F. Gascon, J.-P. Gastellu, L. Jiang,  
1823 A. Kuusk, P. Lewis, X. Li, W. Ni-Meister, T. Nilson,  
1824 P. North, W. Qin, L. Su, R. Tang, R. Thompson, W. Ver-  
1825 hoef, H. Wang, J. Wang, G. Yan, and H. Zang, The RA-  
1826 diation transfer Model Intercomparison (RAMI) exercise:  
1827 Results from the second phase, *Journal of Geophysical Re-*  
1828 *search*, 109, D06210, doi:10.1029/2004JD004252, 2004b.

1829 Pinty, B., T. Lavergne, R. E. Dickinson, J.-L. Wid-  
1830 lowski, N. Gobron, and M. M. Verstraete, Simplifying  
1831 the interaction of land surfaces with radiation for re-  
1832 lating remote sensing products to climate models, *Jour-*  
1833 *nal of Geophysical Research*, 111(D02116), D02,116,  
1834 doi:10.1029/2005JD005,952, 2006.

1835 Prusinkiewicz, P., and A. Lindenmayer, *The Algorithmic*  
1836 *Beauty of Plants*, 240 pp., Springer Verlag, New York, 1990.

1837 Qin, W., and S. A. W. Gerstl, 3-D scene modeling of semi-  
1838 desert vegetation cover and its radiation regime, *Remote*  
1839 *Sensing of Environment*, 74, 145–162, 2000.

1840 Qin, W., and Y. Xiang, An analytical model for bidirectional  
1841 reflectance factor of multicomponent vegetation canopies,  
1842 *Science in China (Series C)*, 40, 305–315, 1997.

1843 Rangasayi, H. N., D. Crisp, S. E. Schwartz, G. P. Anderson,  
1844 A. Berk, B. Bonnel, O. Boucher, F.-L. Chang, M.-D. Chou,  
1845 E. E. Clothiaux, P. Dubuisson, B. Fomin, Y. Fouquart,  
1846 S. Freidenreich, C. Gautier, S. Kato, I. Laszlo, Z. Li,  
1847 J. H. Mather, A. Plana-Fattori, V. Ramaswamy, P. Ric-  
1848 chiazzi, Y. Shiren, A. Trishchenko, and W. Wiscombe, In-  
1849 tercomparison of shortwave radiative transfer codes and  
1850 measurements, *Journal of Geophysical Research*, 110, doi:  
1851 10.1029/2004JD005293, 2005.

1852 Rautiainen, M., P. Stenberg, N. T., and A. Kuusk, The ef-  
1853 fect of crown shape on the reflectance of coniferous stands,  
1854 *Remote Sensing of Environment*, 89, 41–52, 2003.

1855 Rochdi, N., R. Fernandes, and M. Chelle, An assessment of  
1856 needles clumping within shoots when modeling radiative  
1857 transfer within homogeneous canopies, *Remote Sensing of*  
1858 *Environment*, 102, 116–135, 2006.

1859 Ross, J., *The Radiation Regime and Architecture of Plant*  
1860 *Stands*, Dr. W. Junk, Boston, 1981.

1861 Saich, P., P. Lewis, M. Disney, and G. Thackrah, Comparison  
1862 of Hymap/E-SAR data with models for optical reflectance  
1863 and microwave scattering from vegetation canopies, in *Pro-*  
1864 *ceedings of Third International Workshop on Retrieval of*  
1865 *Bio- and Geo-Physical Parameters from SAR data for*  
1866 *Land Applications*, p. 427, 2001.

1867 Scholes, R. J., P. G. H. Frost, and Y. Tian, Canopy structure  
1868 in savannas along a moisture gradient on Kalahari sands,  
1869 *Global Change Biology*, 10, 292–302, doi:10.1111, 2004.

1870 Sellers, P. J., F. G. Hall, R. Kelly, A. Black, D. Baldocchi,  
1871 J. Berry, M. Ryan, K. J. Ranson, P. M. Crill, D. P. Let-  
1872 tenmaier, H. Margolis, J. Cihlar, J. Newcomer, D. Fitzjar-  
1873 rald, P. G. Jarvis, S. T. Gower, D. Halliwell, D. Williams,  
1874 B. Goodison, D. E. Wickland, and F. E. Guertin, BOREAS  
1875 in 1997: Experiment overview, scientific results and future  
1876 directions, *Journal of Geophysical Research*, 102, 28,731–  
1877 28,770, 1997.

1878 Shultis, J. K., and R. B. Myneni, Radiative transfer in vegeta-  
1879 tion canopies with anisotropic scattering, *Journal of Quan-*  
1880 *titative Spectroscopy and Radiation Transfer*, 39, 115–129,  
1881 1988.

1882 Smolander, S., and P. Stenberg, Simple parameterizations of  
1883 the radiation budget of uniform broadleaved and coniferous  
1884 canopies, *Remote Sensing of Environment*, 94, 355–363,  
1885 2005.

1886 Soler, C., and F. Sillion, Hierarchical instantiation for radios-  
1887 ity, in *Rendering Techniques '00*, edited by B. Peroche  
1888 and H. Rushmeier, pp. 173–184, Springer Wien, New York,  
1889 2000.

1890 Stricker, N. C. M., A. Hahne, D. L. Smith, and J. Delderfield,  
1891 ATSR-2: The evolution in its design from ERS-1 to ERS-2,  
1892 *ESA Bulletin*, 83, 32–37, 1995.

1893 Thompson, R. L., and N. S. Goel, Two models for rapidly  
1894 calculating bidirectional reflectance: Photon spread (ps)  
1895 model and statistical photon spread (sps) model, *Remote*  
1896 *Sensing Reviews*, 16, 157–207, 1998.

1897 Tian, Y., Y. Wang, Y. Zhang, Y. Knyazikhin, J. Bogaert,  
1898 and R. B. Myneni, Radiative transfer based scaling of LAI  
1899 retrievals from reflectance data of different resolutions, *Re-*  
1900 *remote Sensing of Environment*, 84, 143–159, 2002.

1901 Verhoef, W., Theory of radiative transfer models applied to  
1902 optical remote sensing of vegetation canopies, Ph.D. thesis,  
1903 Wageningen, 1998.

1904 Verhoef, W., Improved modelling of multiple scattering in leaf  
1905 canopies: The model SAIL++, in *Proceedings of the First*  
1906 *Symposium on Recent Advances in Quantitative Remote*  
1907 *Sensing, Torrent, Spain, September 2002*, edited by A. So-  
1908 brino, pp. 11–20, 2002.

1909 Verhoef, W., and H. Bach, Simulation of hyperspectral and  
1910 directional radiance images using coupled biophysical and  
1911 atmospheric radiative transfer models, *Remote Sensing of*  
1912 *Environment*, 87, 23–41, 2003.

1913 Verstraete, M. M., Radiation transfer in plant canopies:  
1914 Transmission of direct solar radiation and the role of leaf  
1915 orientation, *Journal of Geophysical Research*, 92, 10,985–  
1916 10,995, 1987.

1917 Verstraete, M. M., Radiation transfer in plant canopies: Scat-  
1918 tering of solar radiation and canopy reflectance, *Journal of*  
1919 *Geophysical Research*, 93, 9483–9494, 1988.

- 1920 Weber, J., and J. Penn, Creation and rendering of realistic  
1921 trees, in *Proceedings of the 22nd annual conference on*  
1922 *Computer graphics and interactive techniques*, pp. 119–  
1923 128, ACM press, New York, NY, USA, 1995.
- 1924 Widlowski, J.-L., B. Pinty, N. Gobron, M. M. Verstraete, and  
1925 A. B. Davis, Characterization of surface heterogeneity de-  
1926 tected at the MISR/TERRA subpixel scale, *Geophysical*  
1927 *Research Letters*, 28, 4639–4642, 2001.
- 1928 Widlowski, J.-L., B. Pinty, T. Lavergne, M. M. Verstraete,  
1929 and N. Gobron, Using 1-D models to interpret the re-  
1930 flectance anisotropy of 3-D canopy targets: Issues and  
1931 caveats, *IEEE Transactions on Geoscience and Remote*  
1932 *Sensing*, 43, 2008–2017, doi:10.1109/TGRS.2005.853718,  
1933 2005.
- 1934 Widlowski, J.-L., T. Lavergne, B. Pinty, M. M. Verstraete,  
1935 and N. Gobron, Rayspread: A virtual laboratory for rapid  
1936 BRDF simulations over 3-D plant canopies, in *Computational*  
1937 *Methods in Transport*, edited by G. Frank, pp. 211–231,  
1938 ISBN–10 3–540–28,122–3, Lecture Notes in Computational  
1939 Science and Engineering Series, 48, Springer Verlag, Berlin,  
1940 2006a.
- 1941 Widlowski, J.-L., B. Pinty, T. Lavergne, M. M. Verstraete,  
1942 and N. Gobron, Horizontal radiation transport in 3-D for-  
1943 est canopies at multiple spatial resolutions: Simulated im-  
1944 pact on canopy absorption, *Remote Sensing of Environ-*  
1945 *ment*, 103, 379–397, doi:10.1016/j.rse.2006.03.014, 2006b.
-

**Table 1.** List of the participating models, their RT implementation type, scene construction approach and main scientific reference, as well as the names of their operators during RAMI-3

Model name	RT formalism	Scene Setup	Reference	Participant
<i>1-D models</i>				
ACRM	analytic + MKC	2-layer PP, SD	<i>Kuusk</i> [2001]	Kuusk A. <sup>1</sup>
MBRF	analytic + hotspot kernel	PP, SD	<i>Qin and Xiang</i> [1997]	Qin W. <sup>11</sup>
Sail++	N+2 stream	PP, SD	<i>Verhoef</i> [1998, 2002]	Verhoef W. <sup>2</sup>
1/2-discret	analytic + DOM	PP, SD	<i>Gobron et al.</i> [1997]	Gobron N. <sup>3</sup>
2-Stream	analytic	PP, SD	<i>Pinty et al.</i> [2006]	Lavergne T. <sup>3</sup>
<i>3-D models</i>				
5Scale	hybrid (GO)	GP, SD	<i>Leblanc and Chen</i> [2001]	Rochdi N. <sup>9</sup> and Leblanc S. <sup>12</sup>
FLIGHT	MC,RT (forward/reverse)	GP, DL or SD	<i>North</i> [1996]	North P. <sup>10</sup>
4SAIL2	hybrid (4 stream + GO)	2-layer PG,FC	<i>Verhoef and Bach</i> [2003]	Verhoef W. <sup>2</sup>
frat	MC,RT (forward)	GP, DL	unpublished	Lewis P. <sup>8</sup> and Disney M. <sup>8</sup>
FRT	hybrid (GO)	GP, SD	<i>Kuusk and Nilson</i> [2000]	Möttus M. <sup>1</sup> and Kuusk A. <sup>1</sup>
DART	RT (forward) + DOM	voxels, SD	<i>Gastellu-Etcheberry et al.</i> [1996, 2004]	Martin E. <sup>5</sup> and Gastellu J-P. <sup>5</sup>
Drat	MC,RT (reverse)	GP, DL	<i>Lewis</i> [1999]; <i>Saich et al.</i> [2001]	Lewis P. <sup>8</sup> and Disney M. <sup>8</sup>
Hyemalis	radiosity approach	GP, OP, DL	<i>Soler and Sillion</i> [2000], and <i>Helbert et al.</i> [2003]	Ruiloba R. <sup>7</sup> , Soler, C. <sup>13</sup> , and Bruniquel-Pinel V. <sup>7</sup>
MAC	hybrid (GO)	GP, SD, FC	<i>Fernandes et al.</i> [2003]	Fernandes R. <sup>9</sup> and Rochdi N. <sup>9</sup>
Rayspread	MC,RT (forward + VR)	GP, DL or SD	<i>Widlowski et al.</i> [2006a]	Lavergne T. <sup>3</sup>
raytran	MC,RT (forward)	GP, DL or SD	<i>Govaerts and Verstraete</i> [1998]	Lavergne T. <sup>3</sup>
RGM	radiosity	GP, DL	<i>Qin and Gerstl</i> [2000]	Xie D. <sup>4</sup>
Sprint3	MC,RT (forward + VR)	GP, SD	<i>Thompson and Goel</i> [1998]	Thompson R. <sup>6</sup>

<sup>1</sup>Tartu Observatory, Tõravere

<sup>2</sup>National Aerospace Laboratory NLR

<sup>3</sup>Joint Research Centre

<sup>4</sup>School of Geography, Beijing Normal University

<sup>5</sup>Centre d'Etudes Spatiales de la Biosphère

<sup>6</sup>Alachua Research Institute

<sup>7</sup>NOVELTIS, France

<sup>8</sup>Department of Geography, University College London

<sup>9</sup>Canada Centre for Remote Sensing, Ottawa

<sup>10</sup>NERC CLASSIC, University of Wales Swansea

<sup>11</sup>Science Systems and Applications, Inc., Greenbelt, Maryland

<sup>12</sup>Centre Spatial John H. Chapman, Saint-Huber, Québec

<sup>13</sup>ARTIS, INRIA, Rhône-Alpes, France

DL	deterministic location of scatterer
DOM	discrete ordinate method
FC	statistical description of foliage clumping
GO	geometric optics
GP	geometric primitives
MC	Monte Carlo approach
MKC	Markov chain
OP	Optic primitive
PP	plane parallel canopy
PG	parametric description of canopy gaps
RT	ray-tracing scheme
SD	statistical distribution of scatterer
VR	variance reduction technique

**Table 2.** Model-to-ensemble dispersion statistics,  $\bar{\delta}_m$  [%] for six 3-D Monte Carlo models in RAMI-2 and RAMI-3

model name	BRF type	discrete scenes		turbid scenes	
		RAMI-2	RAMI-3	RAMI-2	RAMI-3
DART	$\rho_{tot}$	-	-	1.42	1.46
	$\rho_{co}$	-	-	1.80	0.81
	$\rho_{mlt}$	-	-	21.44	2.72
	$\rho_{uc}$	-	-	29.02	2.40
drat	$\rho_{tot}$	1.92	0.55	-	-
	$\rho_{co}$	15.98	1.43	-	-
	$\rho_{mlt}$	3.49	1.14	-	-
	$\rho_{uc}$	72.93	7.47	-	-
FLIGHT	$\rho_{tot}$	1.26	0.97	9.63	1.06
	$\rho_{co}$	19.92	3.08	12.72	1.66
	$\rho_{mlt}$	3.33	2.79	15.40	3.10
	$\rho_{uc}$	32.99	10.80	14.29	4.48
Rayspread	$\rho_{tot}$	-	0.55	-	0.64
	$\rho_{co}$	-	1.42	-	0.69
	$\rho_{mlt}$	-	1.18	-	1.48
	$\rho_{uc}$	-	5.88	-	2.62
raytran	$\rho_{tot}$	1.31	0.60	1.06	0.69
	$\rho_{co}$	10.24	1.38	1.47	0.78
	$\rho_{mlt}$	2.73	1.32	10.29	1.81
	$\rho_{uc}$	32.62	7.20	12.83	3.61
Sprint3	$\rho_{tot}$	1.29	1.01	9.66	0.69
	$\rho_{co}$	9.11	2.12	12.67	0.94
	$\rho_{mlt}$	2.44	1.61	15.27	1.61
	$\rho_{uc}$	31.53	7.94	15.72	3.44

In each case, the averaging was performed over all available structural, spectral, illumination and viewing conditions.

**Table 3.** Major variables defining the structural and spectral properties associated to the 100×100 m<sup>2</sup> “birch stand” scene.

parameter [units]	tree class				
	A	B	C	D	E
tree height [m]	2.5	5.5	8.5	11.5	14.5
LAI/tree [m <sup>2</sup> m <sup>-2</sup> ]	0.751	1.081	1.340	1.575	1.805
crown height [m]	1.237	2.952	4.919	7.137	9.606
crown width [m]	0.611	0.995	1.430	1.937	2.538
trunk height [m]	1.263	2.548	3.581	4.363	4.894
trunk width [m]	0.014	0.033	0.054	0.078	0.107
tree density [stem/ha]	38	507	981	261	13
red leaf reflectance	0.10	0.09	0.08	0.07	0.06
red leaf transmittance	0.06	0.05	0.04	0.03	0.03
red trunk reflectance	0.32	0.31	0.30	0.29	0.28
NIR leaf reflectance	0.49	0.48	0.47	0.46	0.45
NIR leaf transmittance	0.50	0.49	0.48	0.47	0.46
NIR trunk reflectance	0.40	0.39	0.38	0.37	0.36

The reflectance of the Lambertian soil was 0.127 (0.159) in the red (NIR) spectral band. The scattering properties of both leaves and trunks were Lambertian.

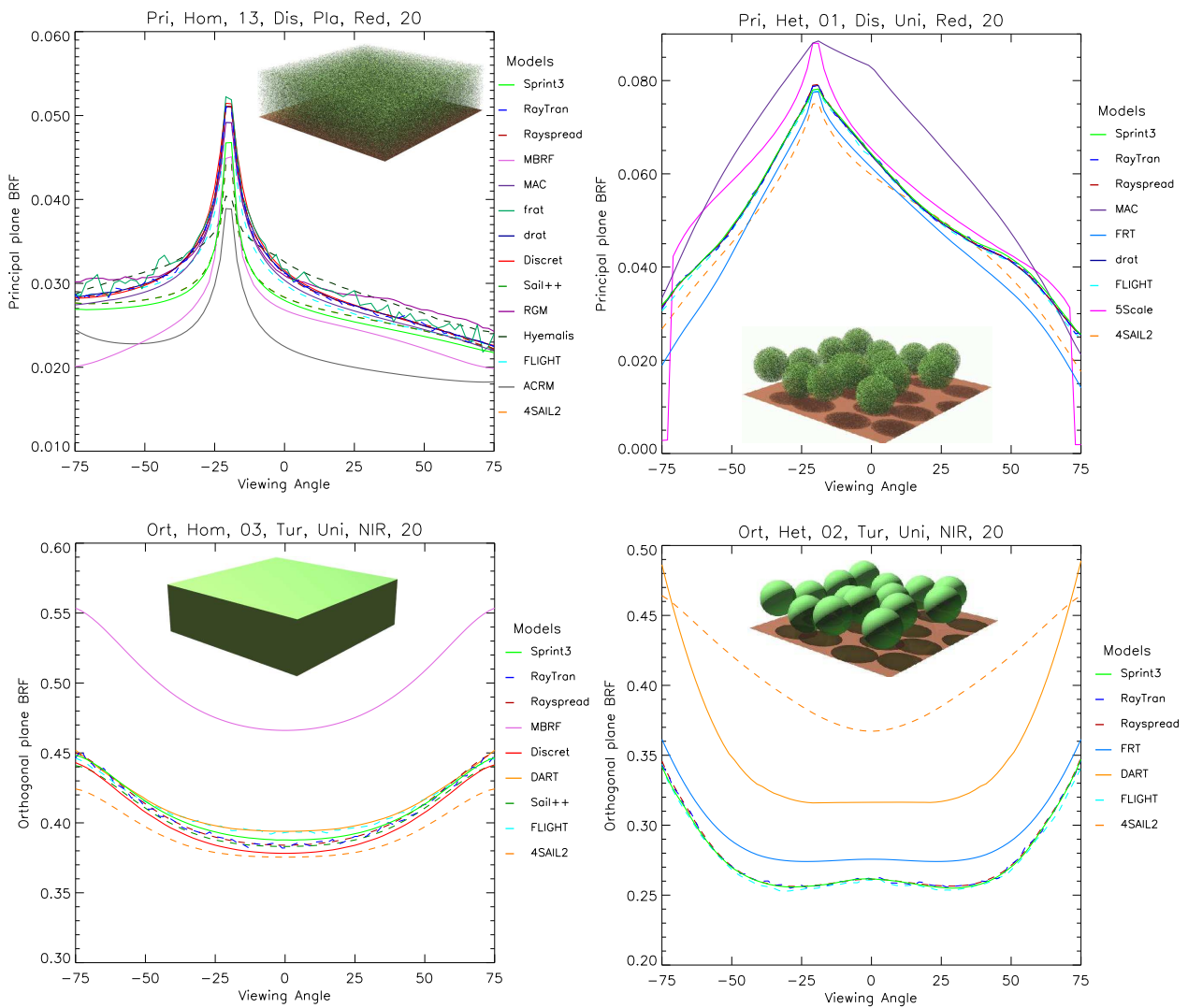


**Figure 1.** Sample BRF results for structurally homogeneous (left panels) and “floating spheres” (right panels) canopies. Model simulations along the principal plane (top panels) relate to test cases with finite-sized scatterers and spectral properties that are typical of the red spectral band. Those along the orthogonal plane (bottom panels) relate to turbid medium foliage representations with spectral properties that are typical of the near-infrared (NIR). The illumination zenith angle was 20° in all cases. Also shown are graphical representations of the various canopy structures.

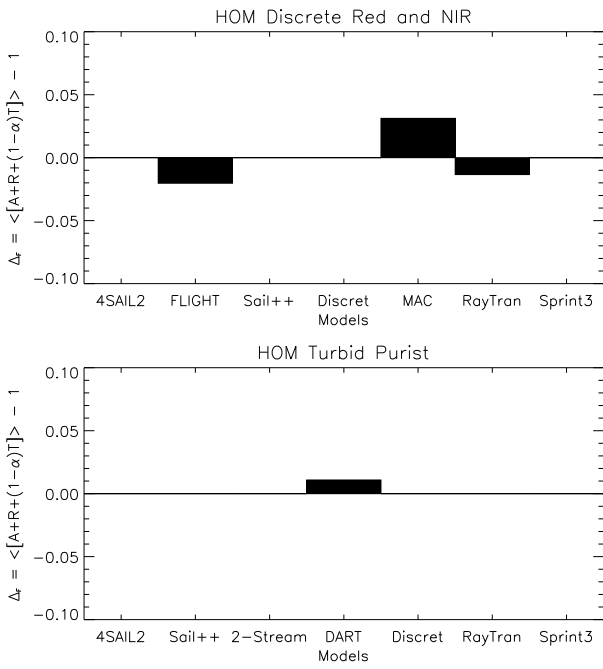


**Figure 2.** The average deviation from energy conservation ( $\Delta_F$ ) for RT models performing 1) the discrete homogeneous baseline scenarios in the solar domain (top panel), and 2) the turbid medium homogeneous test cases under conservative scattering conditions (bottom panel).

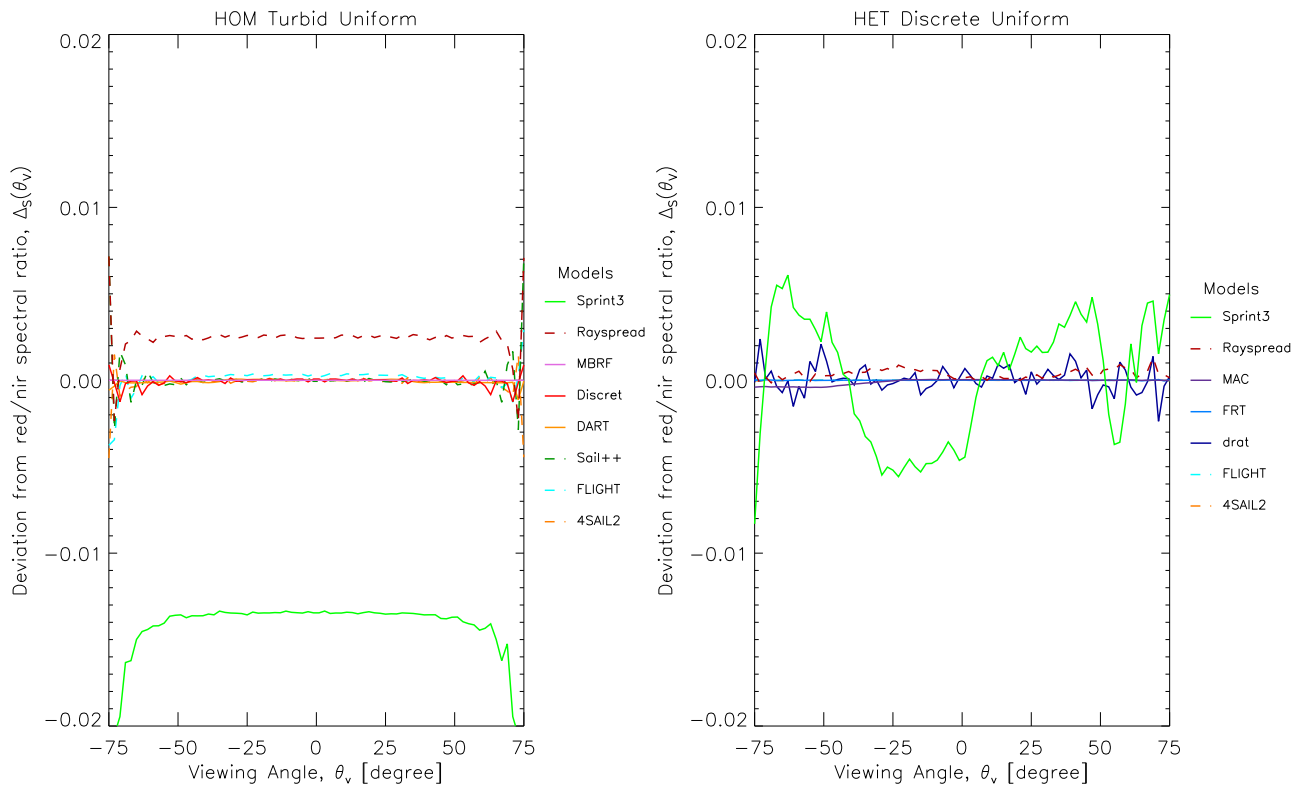


**Figure 3.** Average deviation from the true spectral ratio of the single-uncollided BRF components in the red and NIR spectral domains,  $\Delta_S$ , as a function of view zenith angle for homogeneous turbid medium canopies (left) and discrete floating-spheres canopies (right) with uniform LNDs.

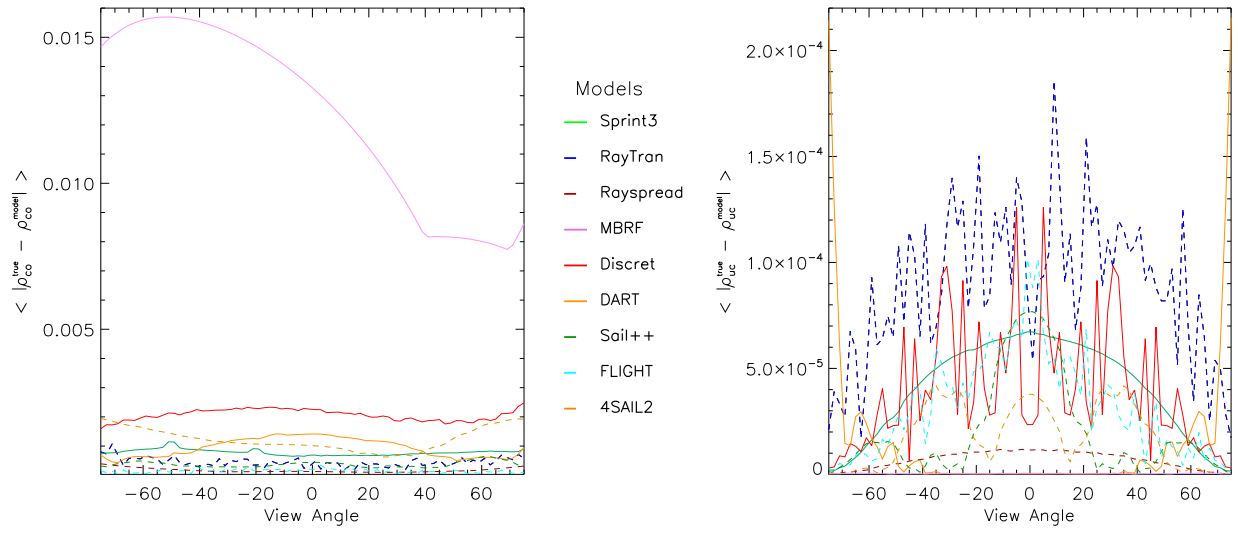


**Figure 4.** The mean absolute error between model simulations and the analytical formulation of the single-collided,  $\rho_{co}$  (left panel) and the single-uncollided,  $\rho_{uc}$  (right panel) BRF components of a homogeneous turbid medium canopy with uniform LND and Lambertian scattering laws. For any view zenith angle the averaging was performed over the principal and orthogonal plane, as well as, for illumination zenith angles of  $20^\circ$  and  $50^\circ$ .

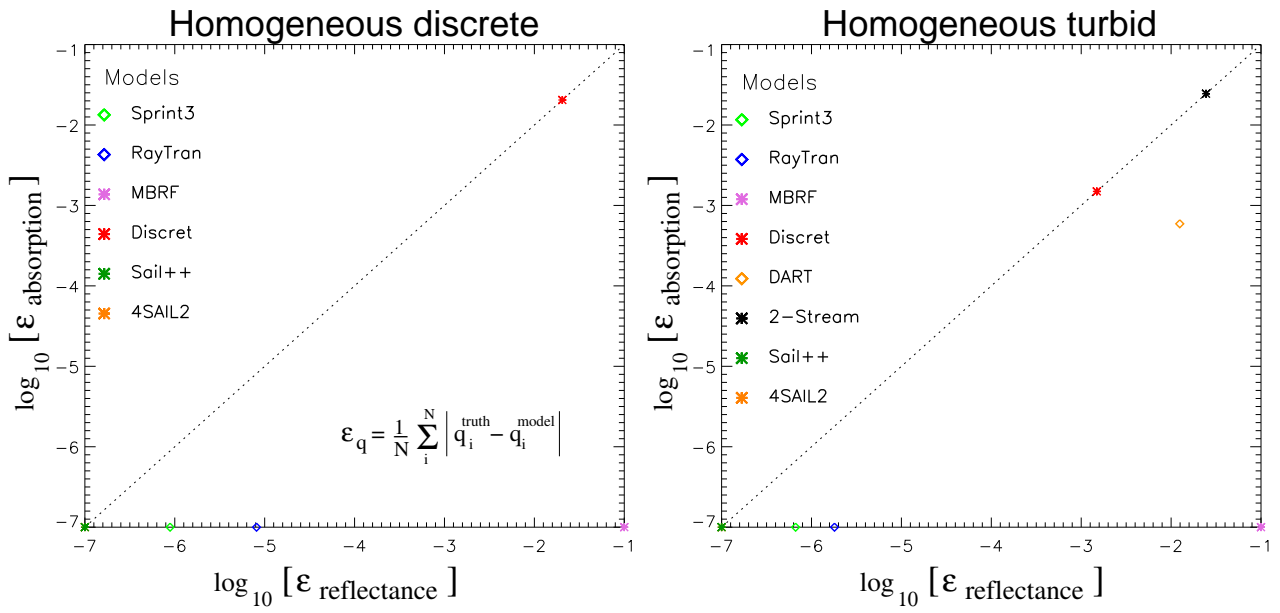


**Figure 5.** The average absolute deviation,  $\varepsilon_q$  between RT model estimates and the true canopy absorption,  $q^{\text{truth}} = A = 0$  (y-axis) or reflectance  $q^{\text{truth}} = R = 1$  (x-axis), on a logarithmic scale, for structurally homogeneous canopies with finite-sized (left panel) and turbid medium (right panel) foliage representations under conservative scattering conditions. The averaging was performed over ( $N = 18$ ) test cases with varying LAI, LND and  $\theta_i$ . Note that—with the exception of MBRF which did not provide absorption estimates—all exact  $A$  and  $R$  values are plotted at  $\log \varepsilon_q = -7$ .

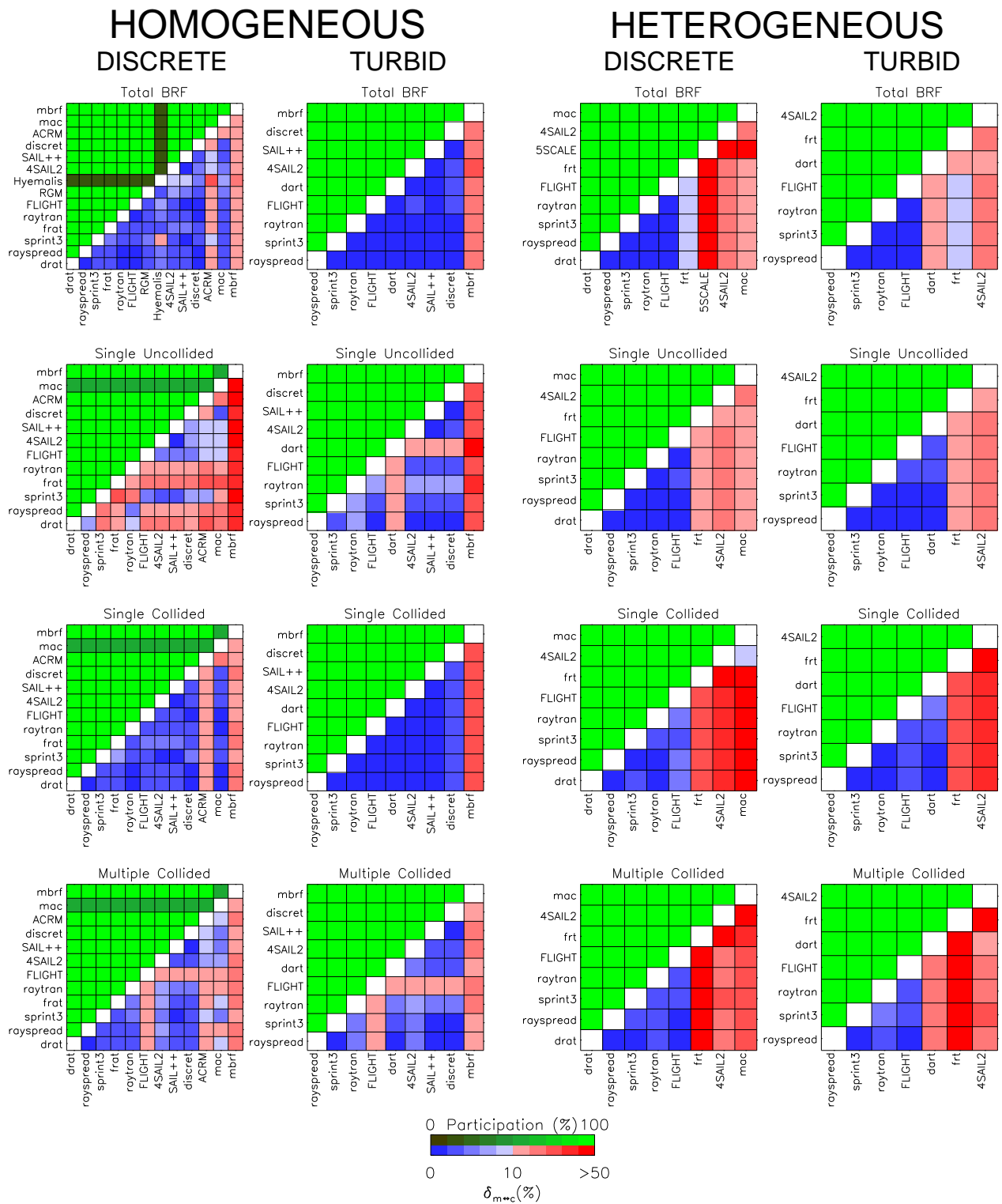


**Figure 6.** Model-to-model differences  $\delta_{m \leftrightarrow c}$  of the total (top row), single-uncollided (second row), single-collided (third row) and multiple-collided (last row) BRF data of models performing the required simulations for structurally homogeneous canopies with finite-sized (leftmost column) and turbid medium (middle-left column) foliage representations, as well as, for “floating spheres” scenarios with finite-sized (middle-right column) and turbid medium (rightmost column) foliage representations in the solar domain. The lower right half of every panel indicates  $\delta_{m \leftrightarrow c}$  in [%] (blue-red colour scheme), whereas the top left half indicates the percentage of available test cases that pairs of models performed together (black-green colour scheme). The green colour scale increments in steps of 10%, the blue in steps of 2% (up to  $\delta_{m \leftrightarrow c} = 10\%$ ), and the red in steps of 10% (with a bright red colour indicating  $\delta_{m \leftrightarrow c} > 50\%$ ).

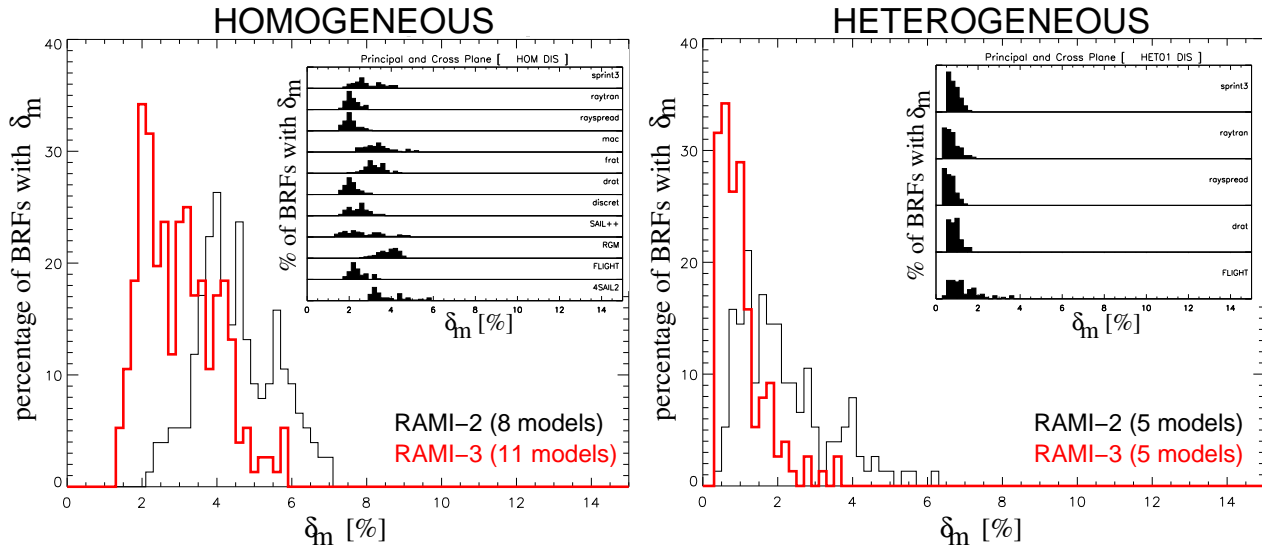


**Figure 7.** The inlaid panels show histograms of model-to-ensemble differences,  $\delta_m$  [%] for selected models participating in the discrete homogeneous (left panel) and discrete “floating spheres” (right panel) test cases. Included in the generation of these histograms are BRF simulations in the principal and orthogonal planes using illumination zenith angles of  $20^\circ$  and  $50^\circ$  in both the red and NIR spectral domain. The main panels show the envelope encompassing the various RAMI-3 (red colour) histograms—shown in the inlaid graphs—in relation to that obtained during RAMI-2 (black line) for the same set of test cases.

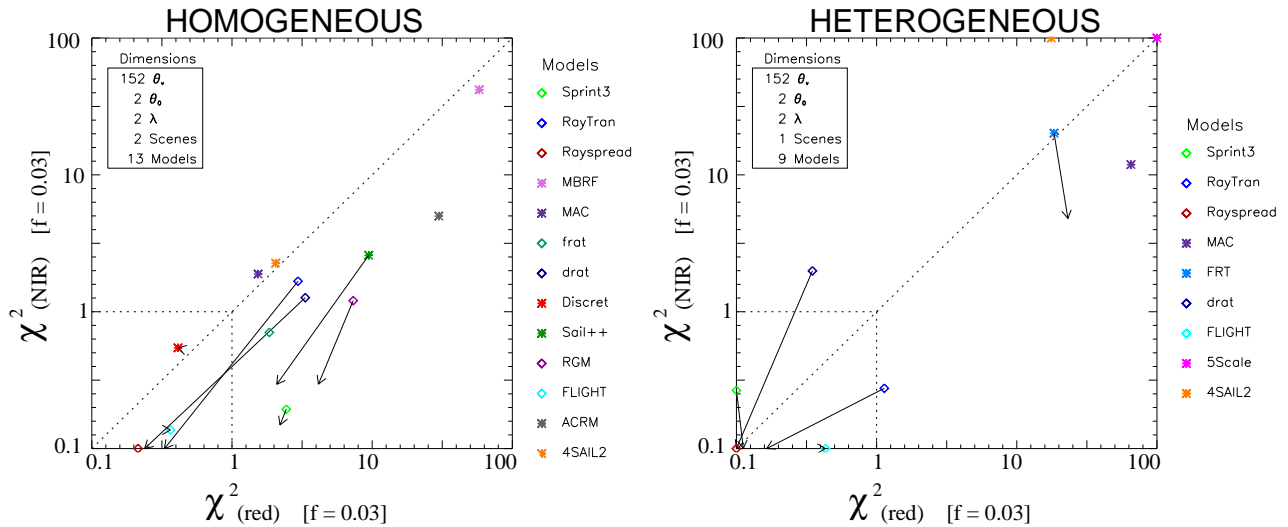


**Figure 8.**  $\chi^2$  statistics in the red (X-axis) and NIR (Y-axis) wavelengths for the structurally homogeneous (left panel) and the “floating spheres” (right panel) baseline scenarios with finite sized scatterers. Arrows indicate changes in the  $\chi^2$  values of models performing both in RAMI-2 (base of arrow) and in RAMI-3 (tip of arrow) using the letter  $\bar{\rho}_{3D}$  as reference.

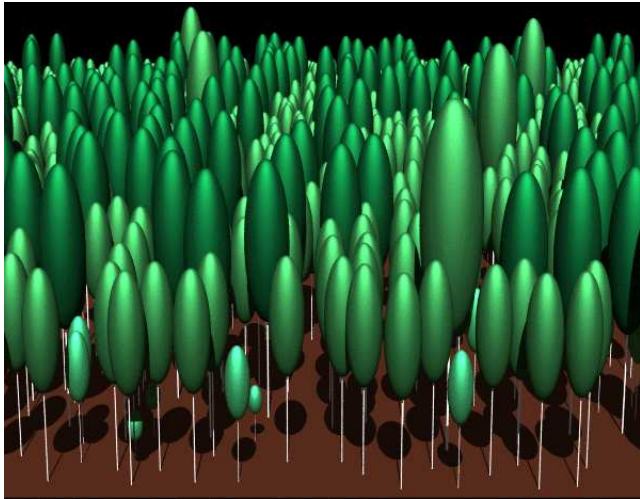


**Figure 9.** Graphical representation of a portion of the RAMI-3 “birch stand” scene when looking from its southern edge in an northward direction towards the centre of the scene. The sun is assumed to be located behind the viewer, *i.e.*, “south” of the scene.

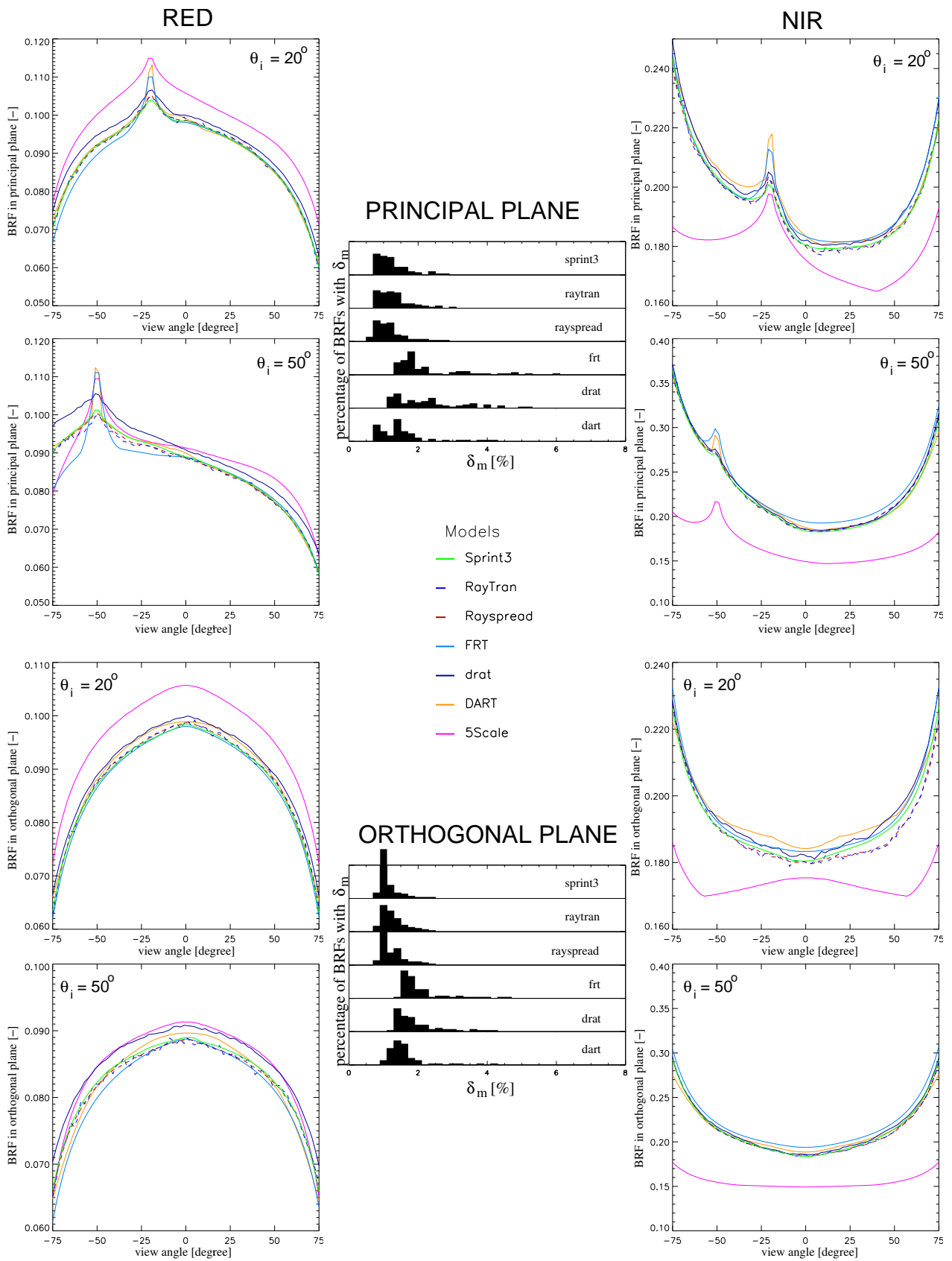


**Figure 10.** Model simulated BRFs in the red (left column) and NIR (right column) spectral domain of the “birch stand” along the principal (upper panels) and orthogonal (lower panels) planes under illumination conditions of  $\theta_i = 20^\circ$  and  $\theta_i = 50^\circ$ . Histograms of model-to-ensemble deviations  $\delta_m$  are provided for (all models but 5Scale in) both observational planes (central panels).

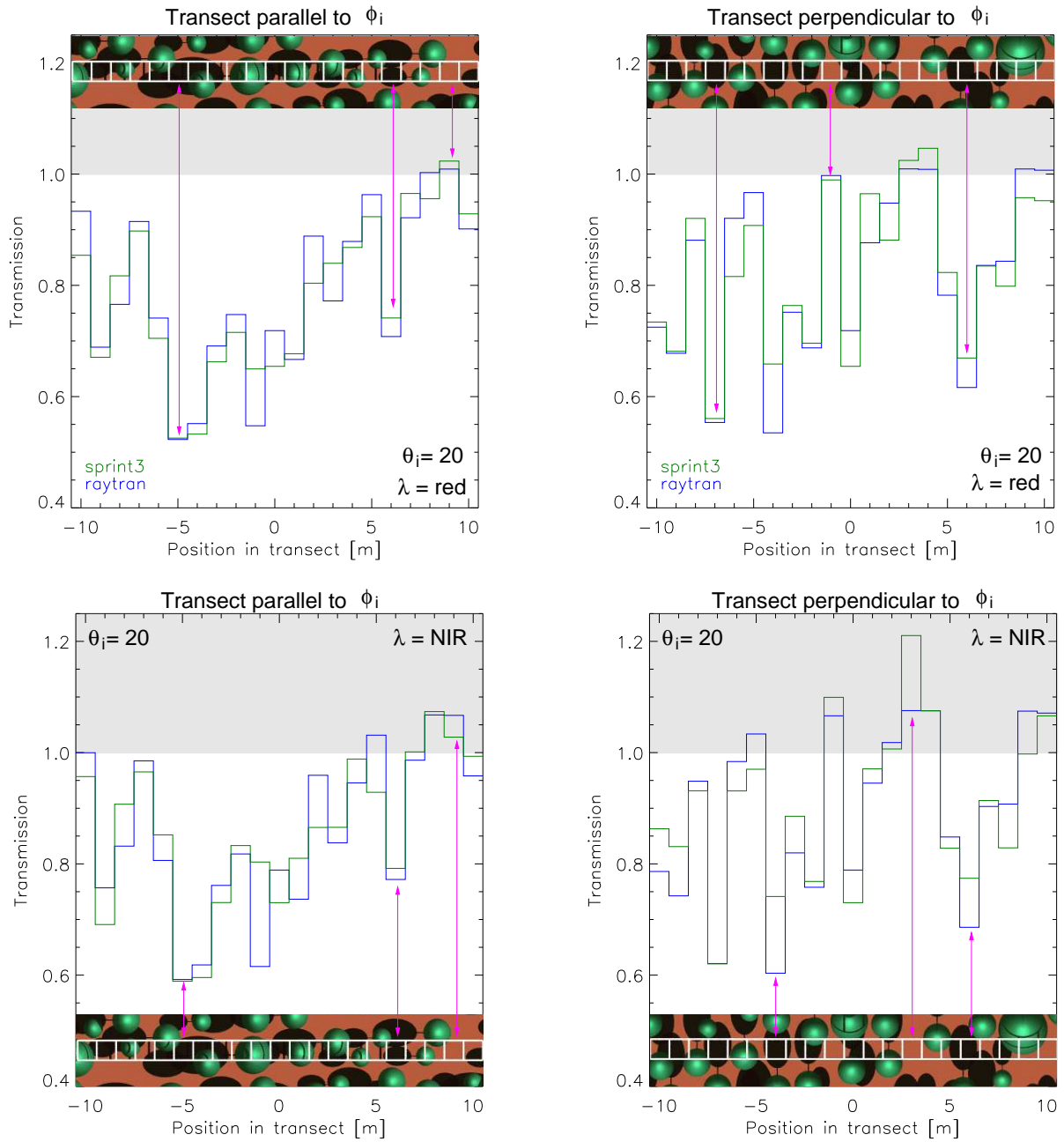


**Figure 11.** Model simulated local transmissions along transects composed of 21 adjacent  $1 \times 1 \text{ m}^2$  patches oriented parallel (left panels) and perpendicular (right panels) to the direction of the illumination azimuth ( $\phi_i$ ) in the red (top panels) and NIR (bottom panels) spectral domain. Pink arrows indicate obvious correlations with predominantly shadowed and illuminated patches in the various graphical representations of the transects (in-laid images featuring the transect as a sequence of white squares). Transmission values that are larger than unity fall within the grey shaded area.

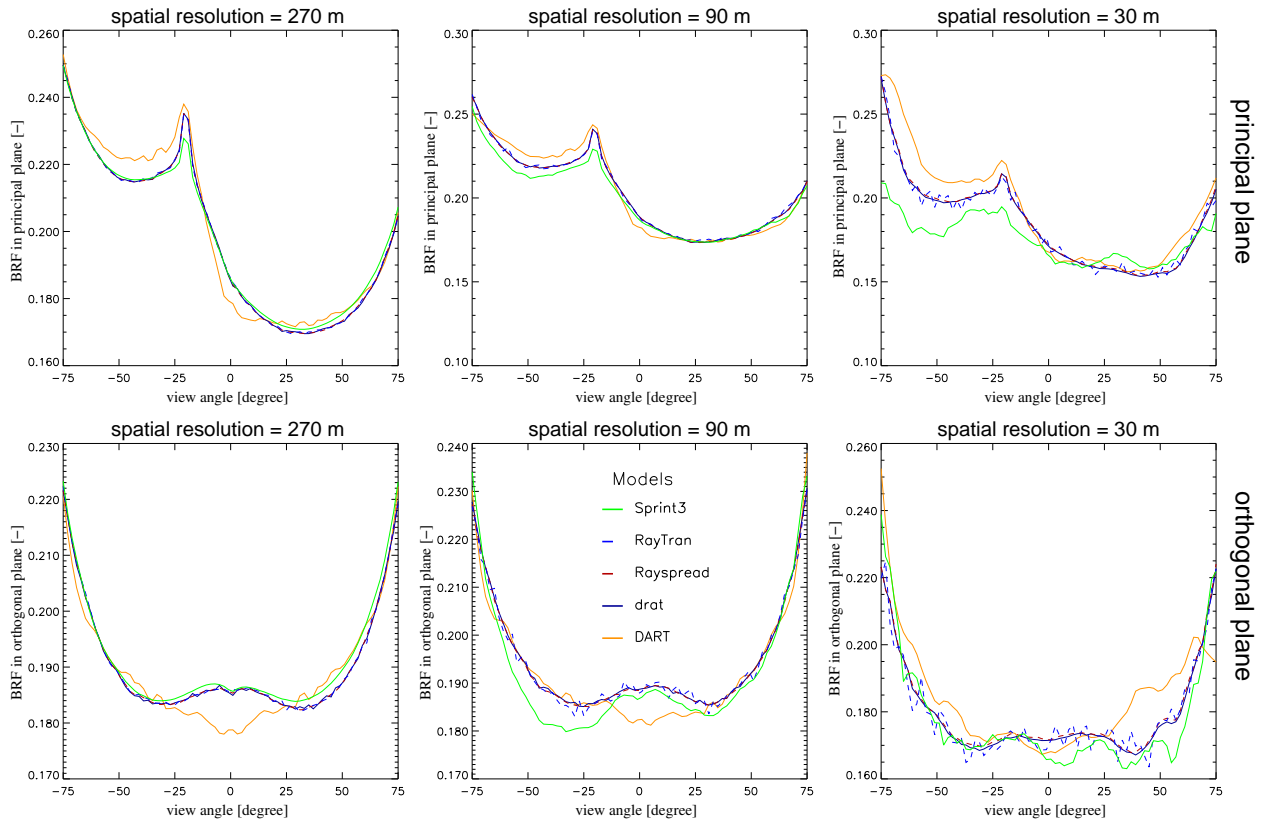


**Figure 12.** Model simulated BRDFs along the principal (top panels) and orthogonal (bottom panels) planes of the “true zoom-in” scene at spatial resolutions of 270 m (left), 90 m (middle) and 30 m (right). The illumination zenith angle was set to  $20^\circ$  and the spectral properties are typical for the NIR spectral domain.

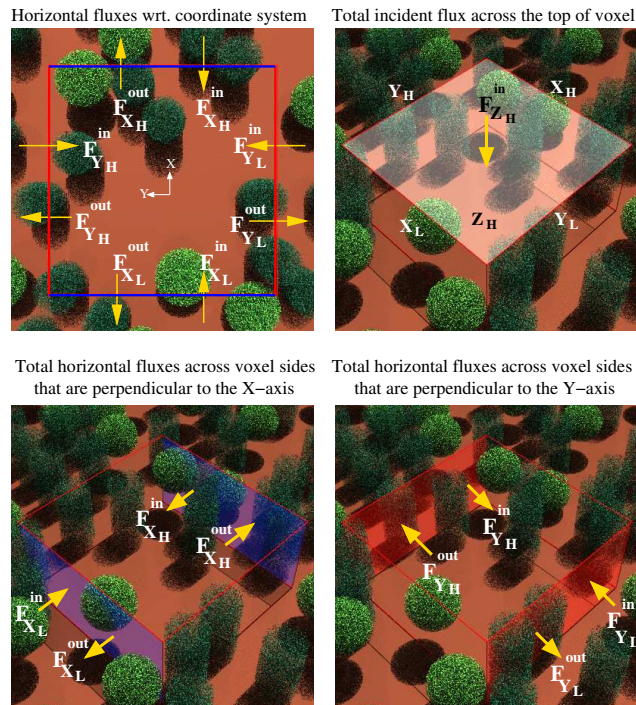


**Figure 13.** Schematics of the various horizontal (and incident) total fluxes entering and exiting a voxel—here of  $30 \times 30 \times 15$  m lateral dimensions—via its lateral (and top) sides. Note that the X-axis is aligned with the azimuthal direction of the incident light.

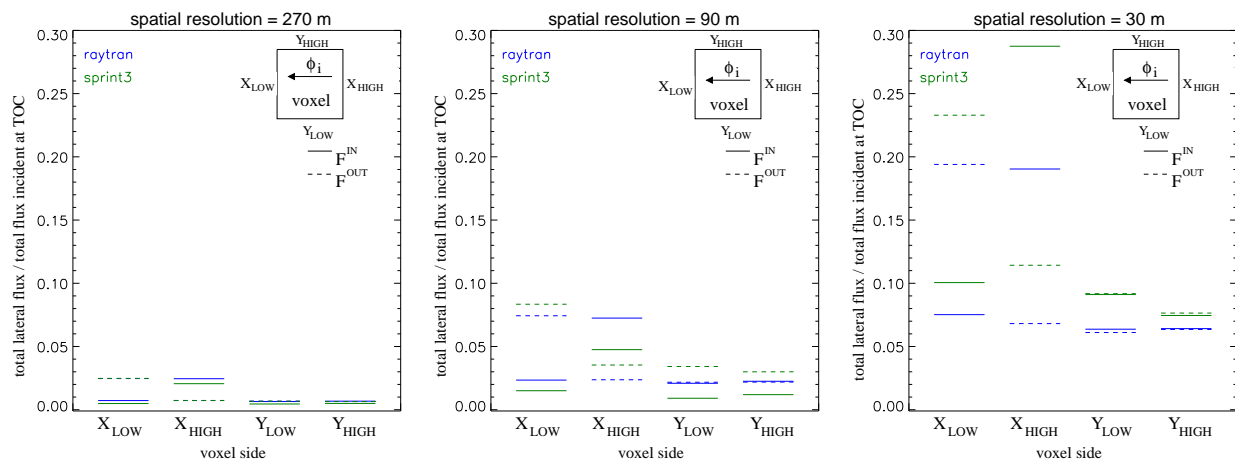


**Figure 14.** Normalised horizontal fluxes entering (solid) and exiting (dashed) the lateral sides of voxels with spatial dimensions equal to 270 m (left), 90 m (middle) and 30 m (right) in the NIR spectral domain. The voxels are centered at the origin of the local coordinate system and have a height of 15 m. The illumination azimuth,  $\phi_i$  is parallel (perpendicular) to the voxel sides labeled  $Y_{LOW}$  and  $Y_{HIGH}$  ( $X_{LOW}$  and  $X_{HIGH}$ ), and  $\theta_i = 20^\circ$ .

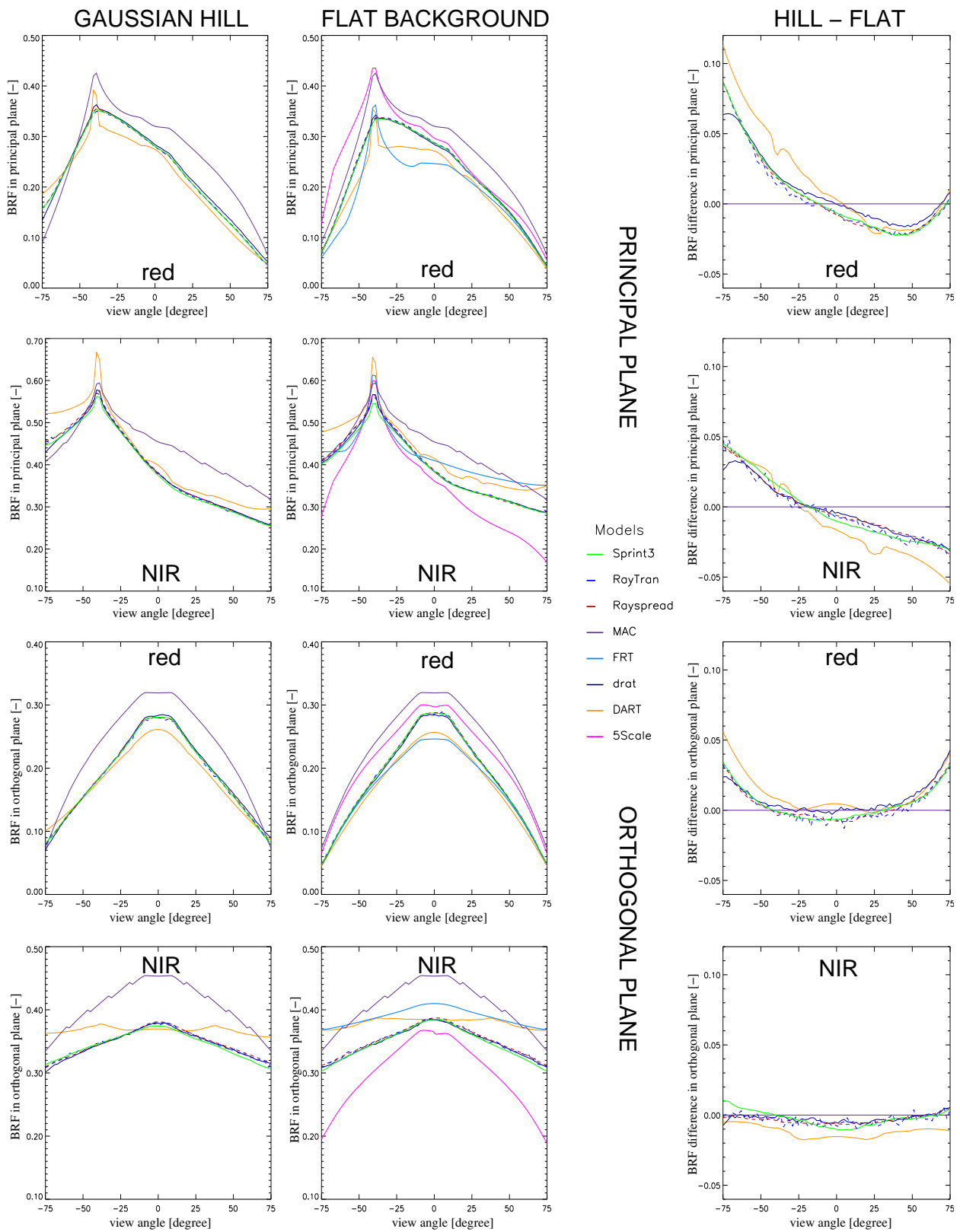


**Figure 15.** Model simulated BRFs in the principal (top 2 rows) and orthogonal (bottom 2 rows) viewing planes for the “conifer forest” scene with topography (left panels), without topography (middle panels), as well as, the difference between these two, respectively (right panels). Simulations pertain to the red (top and third row) and near-infrared (second and bottom row) spectral regimes at  $\theta_i = 40^\circ$ .

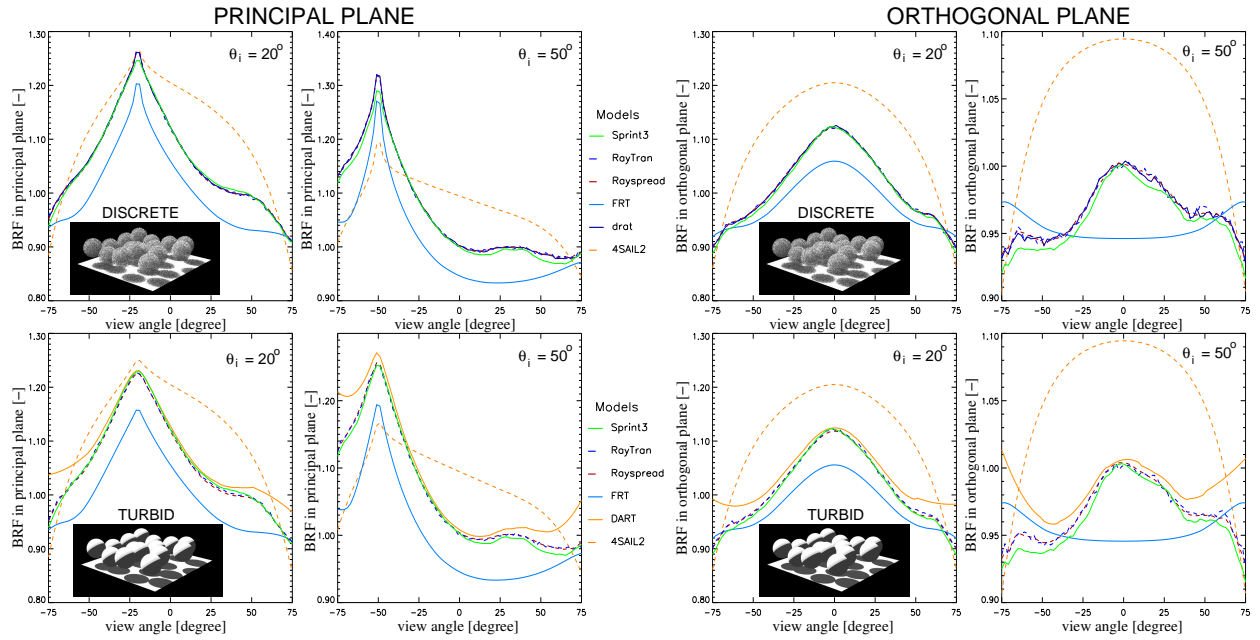


**Figure 16.** Model simulated BRFs for the “floating spheres” scene under conservative scattering conditions (purist corner). Results are shown in the principal (left columns) and orthogonal (right columns) observation planes for discrete (top row) and turbid medium (bottom row) foliage representations and two different illumination zenith angles ( $\theta_i$ ). The structure of the scenes is indicated in the inlaid images.

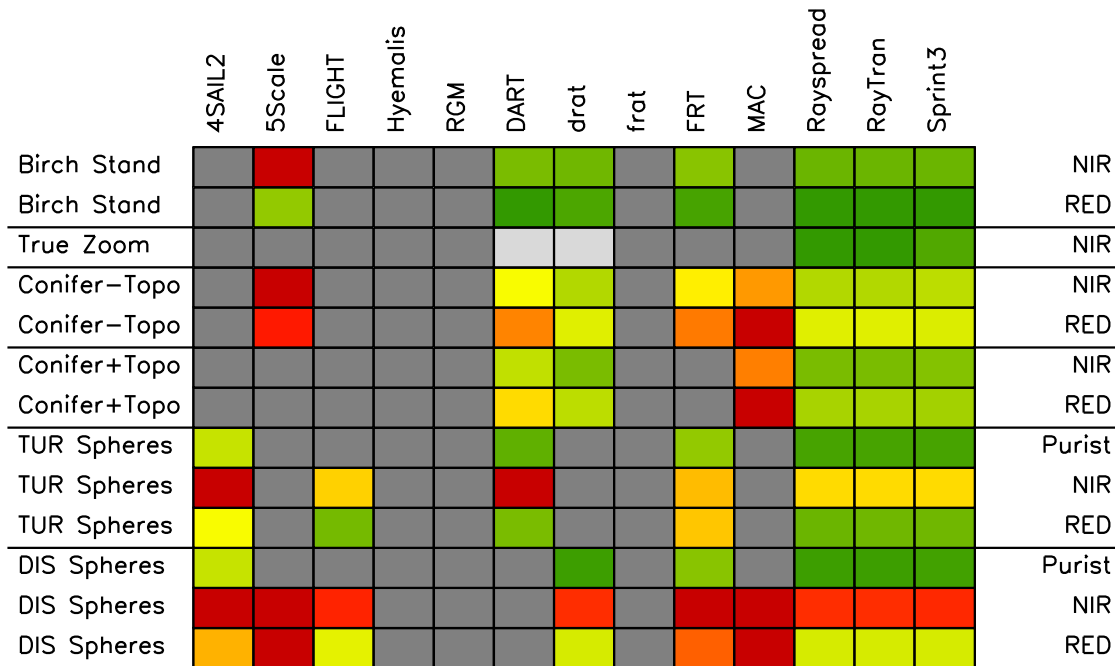
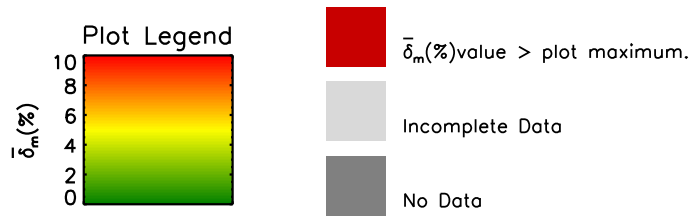
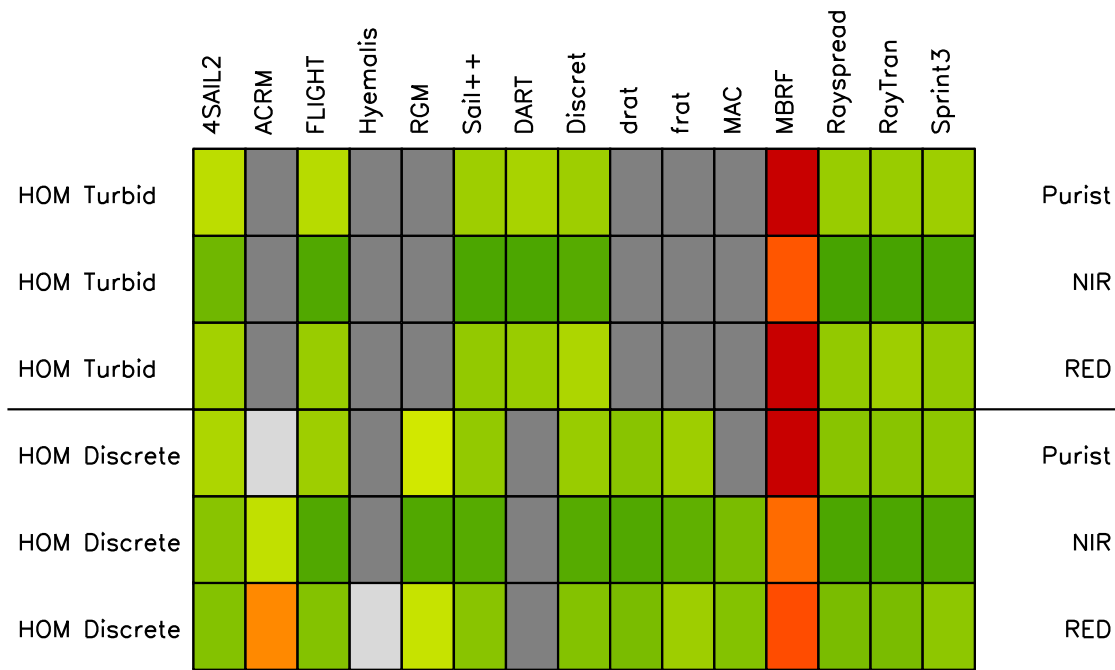


**Figure 17.** Model performance and participation during RAMI-3 for structurally homogeneous (top table) and heterogeneous (bottom table) discrete canopy representation. Model names are listed on the top of each table (one per column). The experiment identifier is provided to the left, the spectral regime to the right, of each table column. Light (dark) grey fields indicate incomplete (no) data submission. The green-yellow-red colour scheme represent the integrated model-to-ensemble difference,  $\bar{\delta}$  [%] obtained with respect to all models that have performed the complete set of prescribed total BRF simulations for any given experiment/spectral regime combination.